Light-driven photothermal catalytic oxidation of toluene over CuO_x-WO_x/$mTiO_{2-x}$-USY: Revealing CuO_x-WO_x synergy

Ehiaghe Agbovhimen Elimian [a,b,c,d], Meng Zhang [a,c,d,f], Qiang Li [a,c,d,f], Jing Chen [e,f], Yong Sun [b], Hongpeng Jia [a,c,d,f,*], Jun He [b,**]

[a] *Xiamen Key Laboratory of Materials for Gaseous Pollutant Control, Institute of Urban Environment, Chinese Academy of Sciences, Xiamen 361021, China*
[b] *Department of Chemical and Environmental Engineering, University of Nottingham Ningbo China, Ningbo 315100, China*
[c] *CAS Center for Excellence in Regional Atmospheric Environment, Institute of Urban Environment, Chinese Academy of Sciences, Xiamen 361021, China*
[d] *Key Laboratory of Urban Pollutant Conversion, Institute of Urban Environment, Chinese Academy of Sciences, Xiamen 361021, China*
[e] *Fujian Institute of Research on The Structure of Matter, Chinese Academy of Sciences, Fuzhou 350002, China*
[f] *University of Chinese Academy of Sciences, Beijing 100049, China*

ARTICLE INFO

ABSTRACT

Light-driven photothermal catalytic oxidation is a promising strategy for sustainable volatile organic compounds (VOCs) elimination. Herein, we report the construction of $yCuO_x$-WO_x/$mTiO_{2-x}$-USY nanocomposite (y = Cu weight percentage and x represents oxygen ratio in metal oxides due to the mixed-valence metal, USY = ultrastable Y zeolite) for the degradation of toluene. Combining both CuO_x and WO_x metal oxides on the $mTiO_2$/USY induced strong light absorption, improved oxygen mobility, and good catalytic activity. Among the catalysts, the optimized $20CuO_x$-WO_x/$mTiO_{2-x}$-USY exhibits the highest light-driven catalytic performance of 90.4% toluene conversion and 82.0% CO_2 yield at a surface temperature of 235 °C under full light irradiation with an optical intensity of 500 mW/cm^2. The existence of a CuO_x-WO_x synergy amplified the capture of light energy, heat generation, and molecular oxygen activation. Impressively, the catalyst demonstrated satisfactory stability during long-term application. Furthermore, *in situ* DRIFTS analysis suggested benzoate species as major reaction intermediates.

1. Introduction

Volatile organic compounds (VOCs) emissions are reactive gases that cause the formation of secondary organic aerosol and ground-level ozone, both of which are harmful to the environment and human health [1]. VOCs can be effectively degraded through catalytic oxidation, although this method relies heavily on nonrenewable energy sources, prompting the need urgency to develop more ecofriendly techniques [2]. Photocatalytic oxidation is an ecofriendly approach for the oxidation of low-concentration VOCs under solar irradiation, although sluggish reaction kinetics and rapid recombination of charge carriers lower the efficiency [3]. Recently, light-driven photothermal catalytic oxidation has emerged as an effective technology for the removal of VOCs by combining the merits of both photocatalytic and thermal catalytic systems. This technique improves the oxidation of

organic pollutants by the efficient capture of photons from the full solar spectrum to elevate the temperature of the catalyst surface. On one hand, the thermal energy generated triggers and drives the catalytic process without the requirement of an external source of heat, whereas traditional photocatalysis contributes by generating charge carriers that participate in the formation of reactive oxygen species and accelerate the oxidative reaction. Hence light-driven photothermal catalysis overcomes the challenges of high energy consumption and slow reaction kinetics displayed by typical thermal catalytic and photocatalytic systems.

Metal nanoparticles such as platinum and silver exhibit localized surface plasmon resonance (LSPR), a collective resonant oscillation of electrons in response to incident light, result in substantial enhancement of photon interactions at the metal surface [4]. Consequently, the LSPR effect can increase cross-section light absorption ability and improve the

* Corresponding author at: Xiamen Key Laboratory of Materials for Gaseous Pollutant Control, Institute of Urban Environment, Chinese Academy of Sciences, Xiamen 361021, China.
** Corresponding author.
E-mail addresses: hpjia@iue.ac.cn (H. Jia), Jun.He@nottingham.edu.cn (J. He).

solar energy utilization efficiency, which is ideal for photothermal catalytic oxidative removal of VOCs. However, the expensive upscaling cost and scarcity of noble metals have prompted the search for earth-abundant alternative materials. Non-noble plasmonic nanomaterials, such as copper oxide are relatively cheaper substitutes with rich surface chemistry and high redox potential for the oxidation of organic pollutants. Furthermore, the narrow bandgap of CuO and the strong LSPR effect of Cu NPs cooperatively extend the absorption ability of the Cu-based nanocomposites [5,6]. Galvita and colleagues reported the improved catalytic oxidation of toluene over the CuO-CeO$_2$/γ-Al$_2$O$_3$ bimetallic nanocomposite compared to CuO/γ-Al$_2$O$_3$ and CeO$_2$/γ-Al$_2$O$_3$ due to the presence of different redox groups and the strong interaction between copper oxide and ceria [7]. In another study, Jiang and co-workers synthesized Pt-Cu/TiO$_2$ composites with high photothermal catalytic performance for toluene oxidation [8]. The high performance of the catalyst was attributed to the strong light absorption properties and close interaction between the metal species.

Defective tungsten oxide (WO$_{3-x}$) is another plasmonic semiconductor that displays the LSPR effect, which arises from a significant increase in free charge carriers induced by regulating the number of oxygen vacancies [9]. The oxygen-deficient WO$_{3-x}$ possesses strong light absorption in the 600–1200 nm range making it a good material for light-driven photothermal applications. In a previous study, defective WO$_{3-x}$ nanoparticles reportedly achieved enhanced photothermal catalytic oxidation of acetaldehyde compared to pristine WO$_3$ due to the increase in oxygen vacancy concentration and strong light absorption induced by post-hydrogen thermal treatment [10]. Considering the above points, the fusion of copper and tungsten metal oxides on suitable support can augment the plasmonic LSPR response for adequate photon capture and improved light-driven photothermal performance.

In addition to the active metal oxides, the porous support material has attracted wide attention because of numerous advantageous properties such as large surface area, good tunability and strong interconnected structural framework, which offers abundant surface sites for efficient VOC oxidation [11]. The presence of ordered cavities provides stability and favours the high loading of metal oxide loading onto porous support for the degradation of organic pollutants [12,13]. For instance, Rostammnia and colleagues reported the synthesis of plasmonic AgPd bimetallic nanoparticles onto single-layer carbon nitride [14]. The highly ordered porous aluminosilicate, zeolite is merited with excellent textural properties and has been proven to assist in the separation and stabilization of charge carriers within its cavities through donor-acceptor interactions [15]. For this reason, zeolites are considered a potential support material for efficient photothermal catalytic oxidation of VOCs.

In view of the advantages of porous materials as catalyst support, the application of 0.9Pt-mTiO$_2$/USY for the light-driven photothermal catalytic oxidation of toluene has previously been reported in our previous works [16]. The introduction of Pt nanoparticles (NPs) into the mTiO$_2$/USY lattice increased the amount of oxygen vacancies and improved the photothermal catalytic activity. However, given the high cost of noble metals, the development of robust photothermal catalysts composed of non-noble metal catalysts is highly desired. In this work, series of CuO$_x$-WO$_x$ bimetallic oxides supported on mTiO$_2$/USY (*y*CuO$_x$-WO$_x$/mTiO$_{2-x}$-USY), were synthesized and applied for the light-driven photothermal catalytic oxidative removal toluene under dry and humid conditions. The novel CuO$_x$-WO$_x$ synergy was elucidated by exploring light absorption, localized surface temperature and mobility of oxygen species. Furthermore, *in situ* DRIFTS analysis suggested that the presence of Cu$^+$/Cu^{2+} and W^{5+}/W^{6+} active sites improve the activation of oxygen and toluene molecules. This study provides insights into elementary occurrences that promote the functionality of bimetallic nanomaterials with broad light absorption ability and catalytic active components for the efficient degradation of VOCs.

2. Experimental section

2.1. Chemicals and materials

Sodium hydroxide (NaOH, 96%), hydrogen peroxide (H$_2$O$_2$, 30% aqueous solution), sodium tungstate dihydrate (Na$_2$WO$_4$·2 H$_2$O, 99.5%), copper nitrate trihydrate (Cu (NO$_3$)$_2$0.3 H$_2$O, 99%), titanium tetraisopropoxide (C$_{12}$H$_{28}$O$_4$Ti, 95%), ethanol absolute (C$_2$H$_5$OH, 99.7%), ethylene glycol (C$_2$H$_6$O$_2$, 99.5%), copper (II) oxide (CuO, 99.0%), tungsten (VI) oxide (WO$_3$, 99.0%), titanium dioxide (P25, 99.8%) were all acquired from Sinopharm Chemical Reagent Co., Ltd. and were of A. R. grade without additional purification.

2.2. Synthesis of mTiO$_2$/USY

The mesoporous TiO$_2$ modified USY (mTiO$_2$/USY) was synthesized in accordance with the following procedure. 1.0 g of USY was added to 2 wt% polyvinyl pyrrolidone (PVP) solution and stirred for 12 h at room temperature. the products were centrifuged and dried at 80 °C overnight in a vacuum oven. Subsequently, the dried samples were calcinated at N$_2$ for 1 h at 400 °C at a heating rate of 2 °C/min to obtain USY/PVP nanocomposite. The USY/PVP powder was dispersed in ethanol and ethylene glycol solution, following the addition of 0.08 g of 1-hexadecylamine (HDA) surfactant, and stirred for 30 mins at room temperature. Then 4 mL of titanium tetra-isopropoxide (TTIP) was added to the solution and stirred for 3 h. The suspension was filtered, washed three times with ethanol and water and dried at 100 °C for 12 h. The dried sample was calcined in air at 400 °C for 4 h and the as-prepared sample was denoted as mTiO$_2$/USY.

2.3. Synthesis of WO$_x$/mTiO$_{2-x}$-USY

First, 0.36 g of Na$_2$WO$_4$·2 H$_2$O were dispersed into 30 mL of ethanol under stirring. Then 5 mL of H$_2$O$_2$ (conc. 30 wt%) was added dropwise into the above solution and continued to stir for 30 mins to obtain solution A. Meanwhile, 1.0 g of mesoporous TiO$_2$ modified USY (mTiO$_2$/USY) was dispersed in 30 mL of ethanol to obtain solution B. After that, solution A was added to solution B and the suspension was thermostatically held at 80 °C for 1 h. The product was collected by centrifugal separation and washed several times with water and ethanol. The collected products were dried at 90 °C for 12 h and then calcined under air at 400 °C for 3 h and subsequently hydrogenated at 600 °C for 2 h to obtain the final product denoted as WO$_x$/mTiO$_{2-x}$-USY nanocomposite. The amount of tungsten ion was calculated theoretically to be 20 wt%.

2.4. Synthesis of CuO$_x$-WO$_x$/mTiO$_{2-x}$-USY

The *y*CuO$_x$-WO$_x$/mTiO$_{2-x}$-USY catalysts were prepared *via* wet impregnation method (Fig. S1). Typically, stoichiometric amounts of Cu (NO$_3$)$_2$0.3 H$_2$O was dissolved in 50 mL of NaOH solution (0.1 M) under magnetic stirring to obtain solution A. Then, 0.36 g of Na$_2$WO$_4$·2 H$_2$O and 1.0 g of mTiO$_2$/USY samples were dispersed in ethanol to obtain solution B. Subsequently, solution A was added to solution B and held thermostatically at 80 °C for 1 h. The products were collected by centrifugation and dried overnight at 90 °C. To introduce surface defect the synthesized catalysts were subjected to post-thermal treatment under pure H$_2$ flow (30 mL/min) for 2 h at 600 °C. The obtained catalysts were denoted as 5CuO$_x$-WO$_x$/mTiO$_{2-x}$-USY, 10CuO$_x$-WO$_x$/mTiO$_{2-x}$-USY, 15CuO$_x$-WO$_x$/mTiO$_{2-x}$-USY, 20CuO$_x$-WO$_x$/mTiO$_{2-x}$-USY and 25CuO$_x$-WO$_x$/mTiO$_{2-x}$-USY. Unsupported CuO$_x$-WO$_x$/mTiO$_{2-x}$ nanocomposites (Cu loading content of 20 wt%) were synthesized for comparison. The real Cu loading contents of all samples were analyzed by using inductively coupled plasma optical emission spectrometry (ICP-OES).

2.5. Characterization of catalyst

Synthesized catalysts were characterized by X-ray diffraction (XRD), Raman spectrometry, scanning electron microscopy (SEM), X-ray photoelectron spectroscopy (XPS), inductively coupled plasma optical emission spectroscopy (ICP-OES), transmission electronic microscopy (TEM), energy dispersive X-ray spectroscopy (EDX) mapping, N_2 adsorption-desorption, UV–Vis-IR absorption spectroscopy, Electrochemical impedance spectroscopy (EIS), Photocurrent, Temperature-programmed desorption of oxygen (O_2-TPD), helium (He-TPD) and toluene (Toluene -TPD) as well as *in-situ* diffuse reflectance infrared Fourier transformed spectroscopy (DRIFTS). The details of the characterization procedures are provided in the Supporting Information.

2.6. Photothermal catalytic evaluation

A 300 W Xenon light (PLS-SXE300/300UV, perfect light) served as a source of irradiation during the photothermal catalytic oxidation of toluene. The catalyst layer was prepared by dissolving 30 mg of the catalyst in 5 mL ethanol. The solution was then filtered onto a fiberglass membrane with a diameter of 50 mm and subsequently dried overnight at 100 °C. The catalytic reaction was conducted in a continuous fixed-bed stainless-steel reactor with an aluminosilicate fiber positioned at the bottom. To observe the surface temperature of the catalyst under irradiation, a thermocouple was placed in the middle of the catalyst layer in the reactor. Adsorption-desorption equilibrium tests were carried out on the catalyst before irradiation. The feed stream was consisted of 200 ppm toluene + 20 vol% O_2 + N_2 (balance gas). The toluene gas was generated by purging liquid toluene with N_2 gas. Subsequently, the produced toluene gas was combined with the balance gas, and the initial concentration of 200 ppm toluene was determined by adjusting the flow rate of N_2 gas and synthetic air through utilization of mass flow meter. The total flow rate was 15 mL/min. For experiments under humid conditions, the 5 vol% water content was introduced into the reaction gas mixture by bubbling N_2 gas through a water saturator at certain temperature.

The photothermal catalytic durability of the catalyst under irradiation from a Xenon light, with a light intensity of 500 mW/cm^2 was carried out in a stainless-steel reactor with a quartz window. A feed stream of 200 ppm toluene + 20 vol% O_2 + N_2 continuously flowed into the reactor at a flow rate of 15 mL/min under irradiation for 12 h. In addition, the stability of the catalyst was investigated by cycling test under light irradiation. After each cycle of the photothermal catalytic test, the continuous toluene feed stream is turned off and the reactor is purged with air to remove products. Subsequently, the continuous

reaction feed is turned on and the next catalytic test begins under irradiation with each cycle lasting 90 mins. A GC 9160 gas chromatograph (GC) fitted with a flame ionization detector (FID) and a thermal conductivity detector (TCD) was used to analyze the reactants and products The performance of the catalyst was analyzed by calculating the toluene conversion and the CO_2 yield using the following equations:

$$toluene\,conversion(\%) = 100 \times \frac{[toluene]_{in} - [toluene]_{out}}{[toluene]_{in}} \quad (1)$$

$$CO_2\,yield(\%) = 100 \times \frac{[CO_2]_{produced}}{[CO_2]_{theoretical}} \quad (2)$$

3. Results and discussion

3.1. Crystal phase composition, surface area, and morphology

In Fig. 1A, the XRD patterns of the catalyst are displayed, with the typical USY zeolite displaying main diffraction peaks at 6.5°, 10.3°, 11.9°, 15.8°, 18.7° and 20.5°. These peaks were retained after the incorporation of metal oxides, which indicates maintenance of the USY structure after the impregnation process. In the multicomponent catalyst, the $WO_x/mTiO_{2-x}$-USY sample presents three main characteristic diffraction lines at 23.12°, 23.58° and 24.38° corresponding to the [002], [020], and [200] crystal planes of monoclinic phase WO_3 (PDF no: 00–043–1035), indicating the successful induction of tungsten ions into the $mTiO_{2-x}$/USY nanocomposite [10]. The monoclinic-WO_3 diffraction peaks were observed to heighten with increased CuO_x loading demonstrating changes in the crystal structure with the incorporation of CuO_x oxide into the $WO_x/mTiO_{2-x}$-USY lattice. Despite the similarity of XRD patterns, the presence of new diffraction peaks with low intensities observed around 53.4° and 56.5° assigned to CuO (PDF-01–080–1917) was observed for $yCuO_x$-$WO_x/mTiO_{2-x}$-USY (y = 10, 15, 20 and 25 wt%) as presented in the enlarged XRD pattern. This suggests the good dispersion of CuO_x species on $WO_x/mTiO_{2-x}$-USY structure even at high CuO_x loading [17].

From the Raman spectra scanned from 100 cm^{-1} to 900 cm^{-1} (Fig. 1B), the characteristic peaks of crystalline WO_3 were displayed at 811 cm^{-1}, 720 cm^{-1}, 329 cm^{-1} and 272 cm^{-1} observed on $WO_x/mTiO_{2-x}$-USY [18]. The broad at 811 cm^{-1} can be assigned to distorted tetrahedral coordinated W−O−W [19], while the peak at 720 cm^{-1} corresponded to W−O−W antisymmetric and stretching vibrations [20]. In addition, at 329 cm^{-1}, the W−O−W bending vibration of bridging oxide ions was identified, confirming the presence of the WO_3 monoclinic phase as shown in the XRD analysis. Moreover, with the introduction of CuO_x species, an increase in area and slight shift of WO_3 peaks at 720 cm^{-1} and
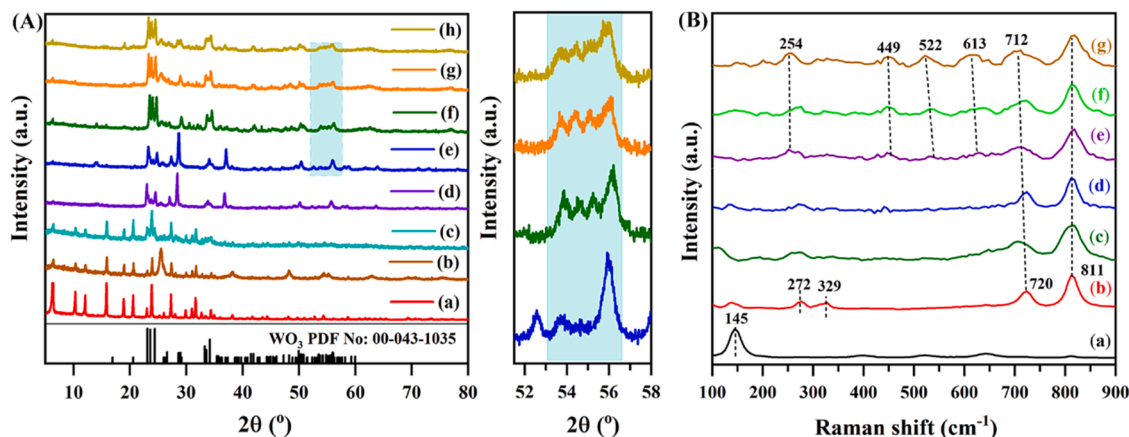
Fig. 1. (A) XRD and (B) Raman Spectra patterns of (a) USY, (b) $mTiO_2$/USY, (c) $WO_x/mTiO_{2-x}$-USY, (d) $5CuO_x$-$WO_x/mTiO_{2-x}$-USY, (e) $10CuO_x$-$WO_x/mTiO_{2-x}$-USY, (f) $15CuO_x$-$WO_x/mTiO_{2-x}$-USY, (g) $20CuO_x$-$WO_x/mTiO_{2-x}$-USY, and (h) $25CuO_x$-$WO_x/mTiO_{2-x}$-USY; (Enlarged XRD pattern of $yCuO_x$-$WO_x/mTiO_{2-x}$-USY with 10, 15, 20 and 25 wt% CuO_x loading, respectively).

272 cm^{-1} to 712 cm^{-1} and 254 cm^{-1} respectively were observed possibly due to the lattice distortion and $CuO_x\text{-}WO_{3-x}$ interaction [21]. The peak at 613 cm^{-1} corresponding to B_g modes of CuO was observed, with other peak points at 450 cm^{-1} and 523 cm^{-1}, indicating the existence of CuO_x species on the surface of $yCuO_x\text{-}WO_x/mTiO_{2-x}$-USY nanocomposites [22].

N_2 adsorption-desorption isotherms and Barrett–Joyner–Halenda (BJH) pore size distributions of the samples are presented in Fig. S2, and their textural properties are summarized in Table 1. The N_2 isotherms of parent USY zeolite displayed the typical type I isotherm signifying the abundant existence of micropores. Furthermore, the USY exhibited the highest adsorption capacity for N_2 molecules, highlighting the large microporous surface area and high pore volume of the USY zeolite [23]. All USY-supported samples exhibited a typical IV-type isotherm with two hysteresis loops in the P/P_0 ranges of 0.2–0.9 and 0.9–0.99, indicating the existence of a mesoporous structure. As presented in Table 1, the BET-specific surface area and total pore volume of the catalyst decreased after loading of WO_x and $CuO_x\text{-}WO_x$ oxides which can be attributed to the partial blocking of the zeolite mesoporous by the metal oxide species. Nevertheless, the BET-specific surface area of $20CuO_x$--$WO_x/mTiO_{2-x}$-USY ($380.8 \text{ m}^2/\text{g}$) was larger than the unsupported $CuO_x\text{-}WO_x/mTiO_{2-x}$ ($64.9 \text{ m}^2/\text{g}$), establishing the USY support functional role in enhancing the surface area. According to the pore size distribution, the pore size of the USY-supported samples falls within the size range of 2–20 nm, with the average pore diameter increasing with metal specie loading. The increase in pore diameter can be attributed to the theoretical expansion of the lattice parameter with the incorporation of Cu species, considering that Cu^{2+} (0.73 Å) has a higher ionic radius compared to Al^{3+} (0.53 Å) and W^{6+} (0.62 Å) and Ti^{4+} (0.61 Å), as well as the amount of Al^{3+} substituted by metal species on framework [24]. The toluene molecule with a size of 0.67 nm can be adsorbed efficiently on the $yCuO_x\text{-}WO_x/mTiO_{2-x}$-USY nanocomposite based on their pore-size distribution as the mesoporous metal oxides provide additional surface sites for the adsorption and desorption of VOCs [25].

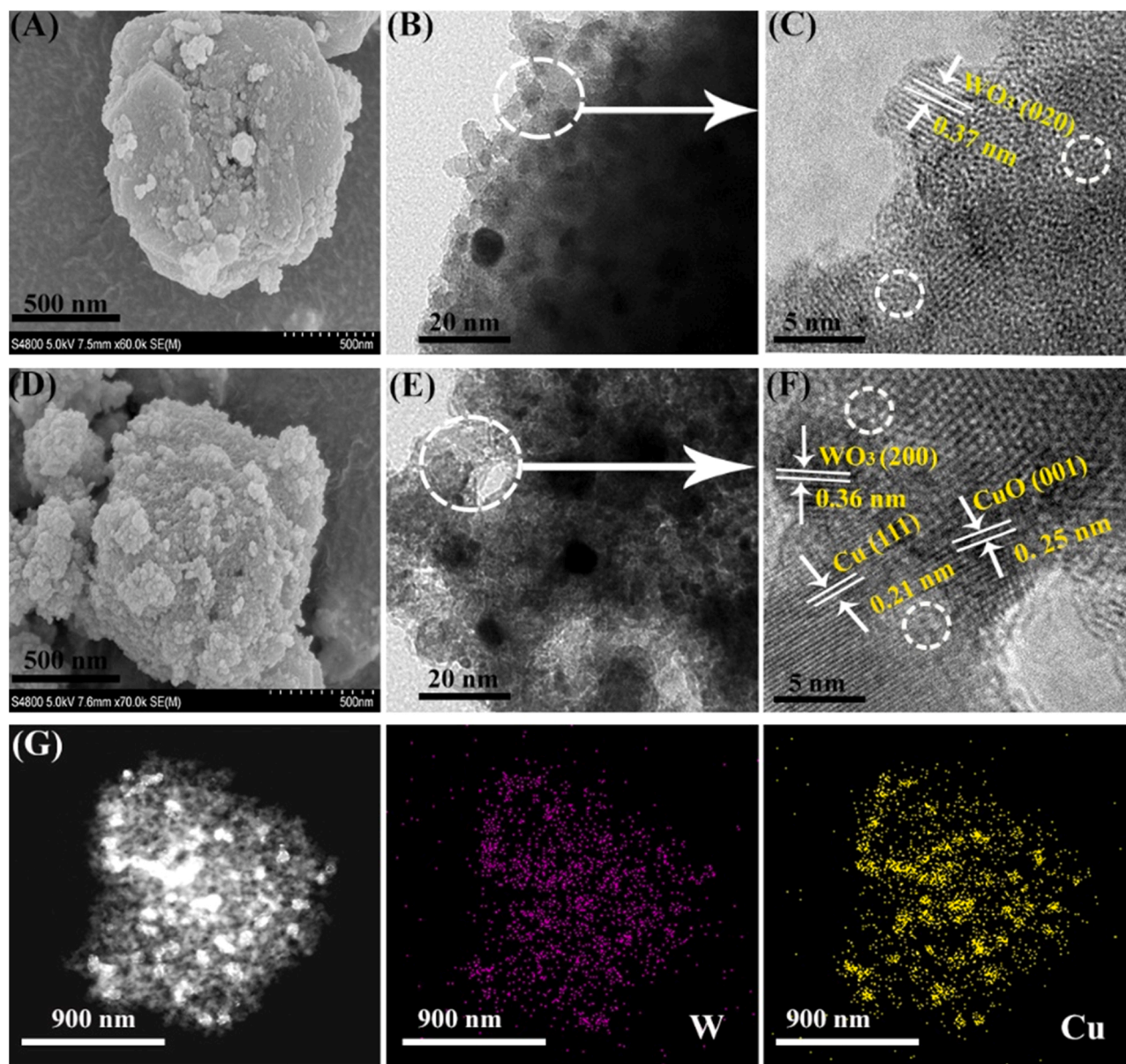The SEM images displayed in Fig S4 and Fig. 2(A and D) provides information about the dispersion of metal oxides on the surface of pure USY, $WO_x/mTiO_{2-x}$-USY and $20CuO_x\text{-}WO_x/mTiO_{2-x}$-USY, respectively. The USY presents an irregular octahedral crystal morphology with a smooth surface. Both $WO_x/mTiO_{2-x}$-USY and $20CuO_x\text{-}WO_x/mTiO_{2-x}$-USY maintain the morphology of USY zeolites, although the $20CuO_x\text{-}WO_x/mTiO_{2-x}$-USY surface appears significantly rougher compared to $WO_x/mTiO_{2-x}$-USY and pure USY zeolite. This can be attributed to the presence of a high amount of CuO_x oxide clusters on the nanocomposite surface. From the HRTEM images of $WO_x/mTiO_{2-x}$-USY (Fig. 2B and C) and $20CuO_x\text{-}WO_x/mTiO_{2-x}$-USY (Fig. 2E and F), the ordered lattice fringes with an interplanar distance of 0.37 nm and 0.36 nm can be assigned to the crystalline of WO_3 (020) and WO_3 (200), respectively [26]. The $20CuO_x\text{-}WO_x/mTiO_{2-x}$-USY also presented the interplanar distance of 0.21 nm and 0.25 nm assigned to the crystal plane of Cu (111) and CuO (011), respectively. The display of apparent defects marked by a white circle was observed in the lattice of $WO_x/mTiO_{2-x}$-USY and $20CuO_x\text{-}WO_x/mTiO_{2-x}$-USY, indicating the existence of oxygen vacancies. Furthermore, as presented in Table 2, EDX analysis was carried out to determine the amount of Cu species present on the surface of $yCuO_x\text{-}WO_x/mTiO_{2-x}$-USY ($y$ = 5.0, 10.0, 15.0, 20.0 and 25.0 wt%). As shown in the Fig. 2G, the EDX elemental mapping images of W and Cu elements indicates the elements distribution of over $20CuO_x\text{-}WO_x/mTiO_{2-x}$-USY. The EDX mapping of other elements such as Al, Si, O and Ti are presented in Fig. S3.

3.2. Surface element composition

The quantitative analysis of the valence states and active species composition of the synthesized samples was explored by XPS spectroscopy. As is shown in Fig. S5, the presence of Ti, O, W and Cu can be observed on the full XPS spectra of the samples. The high-resolution Ti 2p XPS spectrum of the $WO_x\text{-}mTiO_{2-x}$/USY and $yCuO_x\text{-}WO_x/mTiO_{2-x}$-USY samples are shown in Fig. S5 and Fig. 3A, respectively. The Ti 2p spectrum can be fitted into four peaks located at 464.0, 465.1, 459.1 and 458.3 eV, assigned to $Ti^{4+} 2p_{1/2}$, $Ti^{3+} 2p_{1/2}$, $Ti^{4+} 2p_{3/2}$, and $Ti^{3+} 2p_{3/2}$, respectively. The existence of the peak of Ti^{3+} suggests the introduction of Ti^{3+} species into the TiO_2 lattice in the samples through the hydrogen reduction treatment [27]. The O 1 s XPS spectra of samples as shown in Fig. 3B display three deconvoluted peaks at 530, 531, and 532.3 eV assigned to the lattice oxygen (O_{latt}), adsorbed oxygen (O_{ads}), and surface hydroxyl molecules (O_w) [28]. Based on the XPS quantitative analysis, the ratio of O_{ads}/O_{latt} (Table 2) increased with CuO_x metal oxide loading, further indicating the abundance of surface oxygen vacancies for the capture and activation of more surface-adsorbed molecular oxygen. Oxygen vacancies play a key role in enhancing the adsorption and activation of molecular oxygen and reactants on the catalyst surfaces.

The W 4 f XPS spectra of $yCuO_x\text{-}WO_x/mTiO_{2-x}$-USY are displayed in Fig. 3C. The peaks identified at 38.2 and 35.8 eV are assigned to W^{6+} $4 f_{5/2}$ and $W^{6+} 4 f_{7/2}$, while the peaks at 37.0 eV and 34.7 eV belong to the $W^{5+} 4 f_{5/2}$ and $W^{5+} 4 f_{7/2}$ respectively. The existence of W^{5+} species is considered direct proof of the presence of oxygen vacancies in the WO_3 lattice [29]. Interestingly, the relative content of W^{5+} increased slightly with Cu ions introduction compared to the content of $WO_x/mTiO_{2-x}$-USY, suggesting the facile redox reaction of W^{6+} species with cuprous ions during the impregnation process. This results in a strong interaction between WO_x and CuO_x in the nanocomposite and correlates with the XRD and Raman analysis. Furthermore, the Cu 2p spectra (Fig. 3D) display two prominent peaks at 935.2 and 954.4 eV which are readily assigned to the Cu $2p_{3/2}$ and Cu $2p_{1/2}$, respectively. The Cu$2p_{3/2}$ spectra displayed two deconvoluted peaks at 932.7 and 934.7 which could be attributed to the presence of Cu^+ and Cu^{2+} ions [30]. Meanwhile, the shake-up satellites (Sat.) features at 941.0 and 943.6 for Cu $2p_{3/2}$ and 962.7 for Cu $2p_{1/2}$ with energies approximately 10 eV higher than the Cu $2p_{3/2}$ transition can be attributed to the presence of Cu^{2+} ions [31]. As listed in Table 2, the highest ratio of Cu^+/Cu^{2+} was

Table 1

Physical Properties of the parent USY, $mTiO_{2-x}$-USY, $WO_x/mTiO_{2-x}$-USY and $yCuO_x\text{-}WO_x/mTiO_{2-x}$-USY samples.

Sample	BET surface area (m^2/g)	Average pore diameter (nm)	Pore volume (cm^3/g)		Absorptance[a] (a, %)
			V_{Micro}	V_T	
USY	700	2.4	0.32	0.34	12.5
$mTiO_2$/USY	502.2	3.4	0.15	0.25	68.9
$WO_x/mTiO_{2-x}$-USY	469.7	4.69	0.15	0.24	80.8
$5CuO_x\text{-}WO_x/mTiO_{2-x}$-USY	438.8	5.35	0.15	0.24	84.9
$10CuO_x\text{-}WO_x/mTiO_{2-x}$-USY	410.8	6.20	0.14	0.23	86.3
$15CuO_x\text{-}WO_x/mTiO_{2-x}$-USY	397.4	6.70	0.14	0.23	86.7
$20CuO_x\text{-}WO_x/mTiO_{2-x}$-USY	380.8	7.99	0.14	0.23	87.1
$25CuO_x\text{-}WO_x/mTiO_{2-x}$-USY	367.2	8.03	0.14	0.23	88.9
$CuO_x\text{-}WO_x/mTiO_{2-x}$	64.9	10.05		0.18	92.7

Vmicro = micropore volume.

V_T = total pore volume.

[a]Absorptance (a) % = $(\int (1 - A(\lambda)) \times E) / \int E (230 \leq \lambda \leq 2500 \, nm)$.

Fig. 2. (A) SEM images, (B-C) HRTEM images of $WO_x/mTiO_{2-x}$-USY, (D) SEM images and (E-F) HRTEM images of $20CuO_x\text{-}WO_x/mTiO_{2-x}$-USY, (G) EDX elemental mapping (W, Cu) of $20CuO_x\text{-}WO_x/mTiO_{2-x}$-USY.

observed in $20CuO_x\text{-}WO_x/mTiO_{2-x}$-USY. As expected, the catalytic performance of the mixed oxides had a positive relationship with the content of Cu species. The presence of rich Ti^{3+}, W^{5+} and Cu^+/Cu^{2+} species provided evidence of the availability of oxygen vacancies, which is beneficial for the adsorption, and activation of molecular oxygen and reactants [32].

3.3. Light-driven photothermal catalytic performance

Toluene is widely used in industrial processes and chosen as a representative VOC in this study. Fig. 4A and B display the light-driven photothermal performance of the catalyst for the oxidation of toluene. The performance of $WO_x/mTiO_{2-x}$-USY under humid conditions (5 vol % of H_2O) attained 73.9% toluene conversion and 52.6% CO_2 yield. It can be observed that the introduction of Cu ions enhanced the photothermal catalytic activity under the same conditions with $5CuO_x\text{-}WO_x/mTiO_{2-x}$-USY achieving 80.3% and 61.6%, which indicates that the Cu ions are beneficial to toluene oxidation. With the appropriate amount of Cu doping, the $20CuO_x\text{-}WO_x/mTiO_{2-x}$-USY catalyst exhibits the best

catalytic activity with a 90.4% toluene conversion and 82.0% CO_2 yield within 90 min, which is slightly lower than the 92.4% and 85.1% achieved without the addition of water vapour (Fig. S6A and B). Further increasing the amount of CuO_x metal oxide loading to 25% resulted in a slight decrease in the photothermal catalytic activity. The obtained unsupported $CuO_x\text{-}WO_x/mTiO_{2-x}$ nanocomposites exhibit a moderate catalytic performance achieving ∼ 45.8% toluene conversion and 30.9% CO_2 yield after 30 mins of reaction, which rapidly declines to 29.5% toluene conversion and 24.8% after 90 mins reaction time. The steady decline of the photothermal catalytic oxidation of toluene over time can be attributed to the accumulation of reaction intermediates on the catalyst surface, resulting in the blockage of available active sites. These results further establish the merits of the USY support in providing a large surface area and tunable pore structure for the high dispersion of catalytic active species which is conducive in enhancing the photothermal catalytic oxidation of toluene.

For further comparison, the photothermal catalytic activity of commercial TiO_2 (P25), WO_3 and Cu_2O under light irradiation of 500 mW/cm^2 light intensity was investigated. With the surface catalyst

Table 2
Actual Cu continent and surface element compositions of the samples.

Samples	Actual Cu content (wt %)		Surface element composition[a]				
	ICP	EDX	Ti^{3+}/Ti^{4+}	W^{5+}/W^{6+}	Cu^+/Cu^{2+}	$O_{ads}/(O_{latt}+O_w)$	O_{ads}/O_{latt}
$WO_x/mTiO_{2-x}$-USY			0.69	0.43		0.43	0.67
$5CuO_x$-$WO_x/mTiO_{2-x}$-USY	4.7	4.5	0.47	0.46	0.42	0.49	0.72
$10CuO_x$-$WO_x/mTiO_{2-x}$-USY	9.5	7.6	0.53	0.59	0.58	0.50	0.73
$15CuO_x$-$WO_x/mTiO_{2-x}$-USY	14.8	14.2	0.58	0.62	0.70	0.53	0.80
$20CuO_x$-$WO_x/mTiO_{2-x}$-USY	19.6	16.2	0.61	0.68	0.96	0.57	0.84
$25CuO_x$-$WO_x/mTiO_{2-x}$-USY	24.5	23.7	0.67	0.70	0.85	0.62	0.91

[a] Data were estimated by quantitatively analyzing the XPS spectra of the samples.

temperature of TiO_2 (P25), WO_3 and CuO reaching 103.5 °C, 106.0 °C and 131.0 °C respectively, the commercial photocatalysts all displayed extremely low activity as shown in Fig.S7 (A) and (B). The low surface temperatures can be attributed to the poor low light absorption across the whole light spectrum (200–2500 nm) as shown in Fig. S7 (C). On the basis of these experimental results, it can be suggested that efficient absorption of photons and considerable heat generation at the catalyst surface is required to promote the photothermal catalytic oxidation of toluene under these reaction conditions. Moreover, the large surface area, abundant oxygen vacancies and active CuO_x-WO_x metal oxide species contributed to the efficient photothermal catalytic degradation of toluene over $20CuO_x$-$WO_x/mTiO_{2-x}$-USY.To understand such synergistic catalysis processes on CuO_x-WO_x bimetallic oxides, the activity of $20CuO_x/mTiO_{2-x}$-USY was evaluated under the optical intensity of 500 mW/cm^2 (Fig. S8). With the surface catalyst temperature reaching 219 °C, the catalyst achieved a toluene conversion and CO_2 yield of 69.8% and 52. 6% under humid air while a toluene conversion and CO_2 yield of 73.4% and 61.0% were attained under dry air, respectively. This preliminary result suggests that a synergetic interaction between all three components (CuOx, WO_x and TiO_{2-x}) of multifunctional nanocomposites is important for the realization of efficient light-driven thermal catalytic performance. Furthermore, the photothermal catalytic performance of reported catalysts for toluene oxidation are summarized in Table S1 and indicating that $20CuO_x$-$WO_x/mTiO_{2-x}$-USY as an effective photothermal catalyst.

The influence of light intensity on the photothermal catalytic performance of $20CuO_x$-$WO_x/mTiO_{2-x}$-USY for the oxidation of toluene is illustrated in Fig. 4C and D. The photothermal catalytic activity for toluene oxidation over $20CuO_x$-$WO_x/mTiO_{2-x}$-USY correlates favourably with increased optical power density. Under the humid condition, toluene conversion and CO_2 yield were observed to be stable during the 90 min reaction when irradiated intensity is 500 mW/cm^2. However, a decline in photothermal catalytic performance was noted with a reduction in light intensity from 500 to 200 mW/cm^2. A similar trend was observed when toluene photothermal oxidation was carried out in the absence of water vapour (Fig. S9 A and B). According to the above

results, more optical power energy translates into available more light energy for the generation of heat and free charge carriers. Moreover, tracking of catalyst layer surface temperature by a thermocouple verifies the decrease of $20CuO_x$-$WO_x/mTiO_{2-x}$-USY performance with lower light intensities. The following surface temperatures are 235, 232, 223, 218, and 198 °C which corresponds to the light intensity of 500, 450, 400, 300, and 200 mW/cm^2, respectively (Table S2). Based on the above discussion, heat is required to initiate oxidation, and light further accelerates the process.

The region of sunlight spectrum contributing to the photothermal catalytic oxidation of toluene, over $20CuO_x$-$WO_x/mTiO_{2-x}$-USY was investigated by comparing the catalytic activities under UV–vis–IR, UV–vis, and IR regions respectively at a catalyst surface temperature of 235 °C as shown in Fig. 5. Photothermal catalytic activity in the UV-Vis region showed the highest catalytic activity, achieving toluene conversion and CO_2 yield of 97.6% and 91.0%, respectively. The activity under IR irradiation achieved toluene conversion and CO_2 yield of 84.5% and 76.9%, which is higher than the activity without irradiation at 235 °C suggesting that the IR light contributes to the photothermal catalytic activity. Regardless of the light wavelength, the photothermal catalytic performance over $20CuO_x$-$WO_x/mTiO_{2-x}$-USY is higher under irradiation than under heating conditions, which also confirms that light and heat synergy is required for superior catalytic performance. Under light exposure, the localized thermal energy originating from charge carrier recombination and thermal IR effect will be transferred to the active site and provide energy for the reaction, which is crucial for light-driven photothermal catalytic oxidative reactions.

In addition, to verify whether conventional photocatalysis occurs during the reaction, the catalytic activity was performed at a low temperature. The low temperature of 30 °C was achieved by placing the reactor in an ice-water bath. As shown in Fig. S10, under the irradiation, the toluene conversion reached about 10.4% in 6 min and then decreased rapidly, and the CO_2 yield reached 1.7% within the irradiation time. This indicates that $20CuO_x$-$WO_x/mTiO_{2-x}$-USY is a photoactive material capable of generating charge carriers, which is experimentally supported by EIS and transient photocurrent test results (Fig. S11 A and B). In Fig. S11 (A), the $20CuO_x$-$WO_x/mTiO_{2-x}$-USY offers the smallest EIS Nyquist arc radius, indicating that the copper species act as electron acceptors, and enhance interfacial charge mobility. The efficient electron mobility can be ascribed to the reversible redox process between Cu^{2+}/Cu^+ and W^{6+}/W^{5+} occurring on the $20CuO_x$-$WO_x/mTiO_{2-x}$-USY surface [33]. Moreover, the optimized $20CuO_x$-$WO_x/mTiO_{2-x}$-USY displays the highest photocurrent density under intermittent on-off illumination as shown in Fig. S11 (B), which reflects the presence of the increased free charges [34]. The high photocurrent response also validates the restrained recombination of photogenerated carriers with the loading of CuO_x and WO_x on the surface of $mTiO_2$/USY. Hence, the generation efficiency of photogenerated electron-hole pairs prolongs the lifetime of the photo-excited electrons, which increases the probability of electrons participating in surface reactions such as the molecular oxygen activation to produce reactive oxygen species such as superoxide radical (•O_2^-) and hydroxyl radical (•OH). According to the above experiment, the generation of heat energy under irradiation is crucial for the light-driven photothermal degradation of toluene.

The activation and mobility of oxygen species were evaluated by O_2-TPD. According to the desorption temperature of the oxygen species, the O_2-TPD profiles can be separated into three regions: surface chemisorbed oxygen (< 200 °C), surface lattice oxygen (200 – 550 °C) and bulk lattice oxygen (> 550 °C), denoted as α, β and γ, respectively. Furthermore, Fig. 6A shows that the $WO_x/mTiO_{2-x}$-USY sample exhibits broad desorption bands around 142 °C and 780 °C, attributed to the adsorption of oxygen species on the surface oxygen vacancies and lattice oxygen releasing *via* the reduction $W^{6+} \rightarrow W^{5+}$. Interestingly, the desorption peaks of $yCuO_x$-$WO_x/mTiO_{2-x}$-USY samples are mainly concentrated in the surface chemisorbed oxygen desorption region,
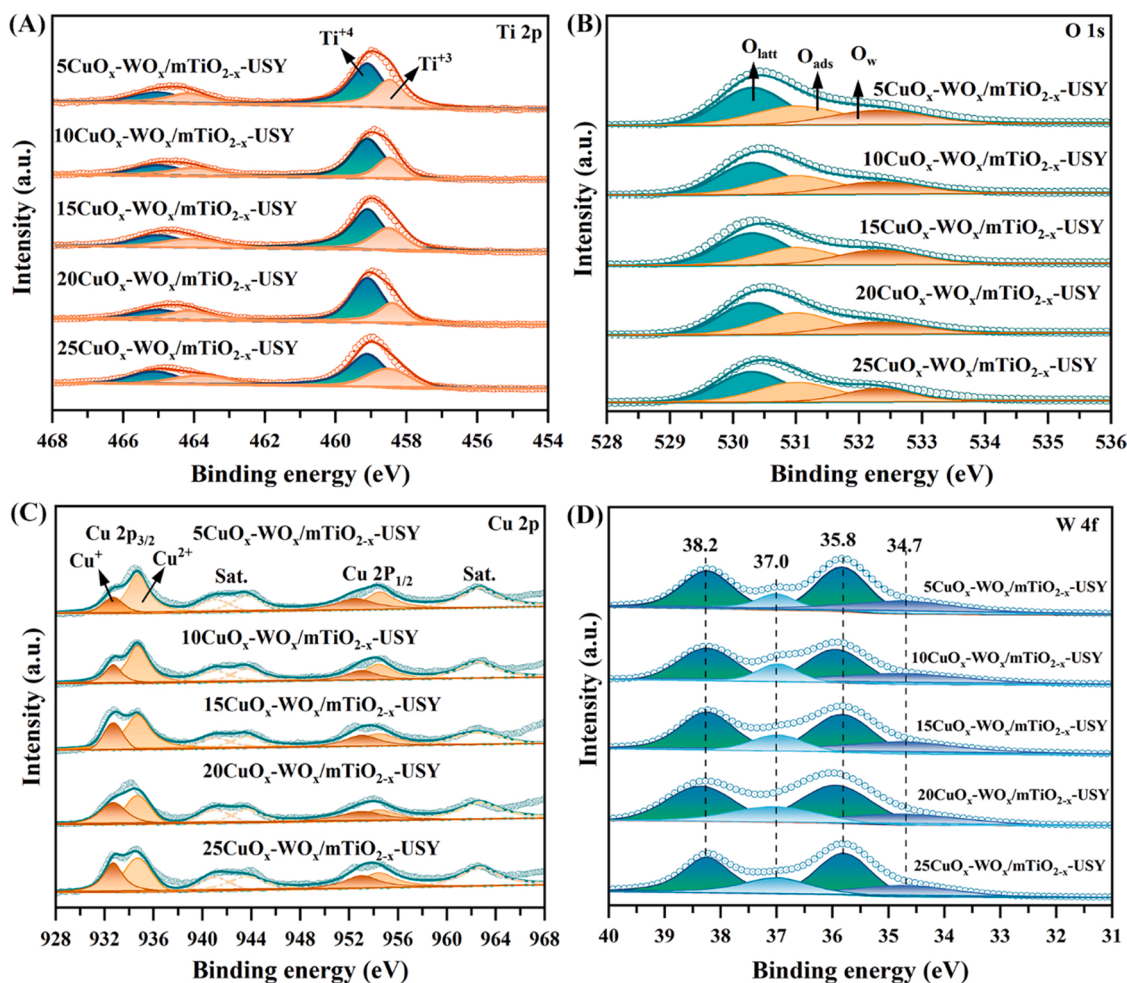
Fig. 3. (A) Ti 2 P (B) O 1 s, (C) Cu 2p and W 4 f XPS spectra of prepared samples.

which shifts to lower temperatures (Table S3), indicating the enhanced mobility of oxygen by the existence of oxygen vacancies and Cu substitution [35]. Furthermore, the improved oxygen mobility and the chemisorbed oxygen on the $yCuO_x$-WO_x/$mTiO_{2-x}$-USY samples suggest the existence of a strong synergistic effect between CuO_x and WO_x. Moreover, the $20CuO_x$-WO_x/$mTiO_{2-x}$-USY displayed significantly broader α peaks within the range of 88 °C and 205 °C as well as Υ peak at 772 °C. The results show that the introduction of copper ions resulted in a remarkable increase in the number of oxygen vacancies, leading to the desorption of more oxygen species [36]. The high concentration of surface-active oxygen species will be beneficial for VOC oxidation.

Toluene-TPD-MS was used to understand the interaction strength between toluene and the as-synthesized hierarchical zeolite samples. The mass spectrometry (MS) signals of toluene were recorded for $m/z = 91$. The addition of tungsten resulted in the display of two peaks on the WO_x/$mTiO_{2-x}$-USY with lower peak intensity. It was observed that the unsupported CuO_x-WO_x/$mTiO_{2-x}$ samples displayed two peaks around 54 °C and 116 °C, which indicates the presence of two adsorption sites. The desorption peak area was reduced in the order of $mTiO_{2-x}$-USY > WO_x/$mTiO_{2-x}$-USY > $5CuO_x$-WO_x/$mTiO_{2-x}$-USY > $10CuO_x$-WO_x/$mTiO_{2-x}$-USY > $15CuO_x$-WO_x/$mTiO_{2-x}$-USY > $20CuO_x$-WO_x/$mTiO_{2-x}$-USY > CuO_x-WO_x/$mTiO_{2-x}$ (Fig. 6B). This result is related to the textural properties listed in Table 1, suggesting that toluene adsorption capacity over the as-synthesized catalyst to closely related to the available specific surface area [37].

However, it is worth noting that the desorption of toluene occurs more easily over $yCuO_x$-WO_x/$mTiO_{2-x}$-USY samples compared to the WO_x/$mTiO_{2-x}$-USY. The toluene desorption peaks shifted to lower

temperatures with elevating amount of CuO_x oxide on the catalyst surface (Table S3), suggesting increased mesoporosity and weakened interaction between toluene-adsorbent interaction [38]. Therefore, in comparison to WO_x/$mTiO_{2-x}$-USY, toluene molecules are easily released from the surface of $20CuO_x$-WO_x/$mTiO_{2-x}$-USY because the loading of CuO_x species weakens the surface interactions and electronic bonds between toluene and USY zeolite. Furthermore, the analysis of the Toluene-TPD-MS profiles suggests that toluene is more facilely adsorbed on the CuO_x site, and the CuO_x-WOx interface promoted the desorption reaction products during the light-driven thermal catalytic reaction.

3.4. Origin of the light-driven photothermal catalytic activity

To further reveal how the intimate association between light-driven photothermal catalysis and light absorption ability promotes the efficient degradation of toluene over $yCuO_x$-WO_x/$mTiO_{2-x}$-USY nanocomposites the UV-Vis-IR absorption spectra of all samples were measured. For comparison, the optical absorption spectra of the defective $mTiO_{2-x}$-USY, WO_x/$mTiO_{2-x}$-USY and unsupported CuO_x-WO_x/$mTiO_{2-x}$ were also measured. As shown in Fig. 7A, the $mTiO_{2-x}$-USY displayed moderate absorption in the entire spectrum after hydrogenation. The addition of tungsten resulted in the extension of light absorption in the visible and IR region which can be attributed to the presence of W^{5+} species and increased abundance of oxygen vacancies through hydrogenation [39]. With the introduction of CuO_x species, an extension in visible and the NIR light region can be observed due to the 3d valence → 4sp conduction inter-band transitions of Cu ions [40]. In addition, the enhanced absorption peaks for the
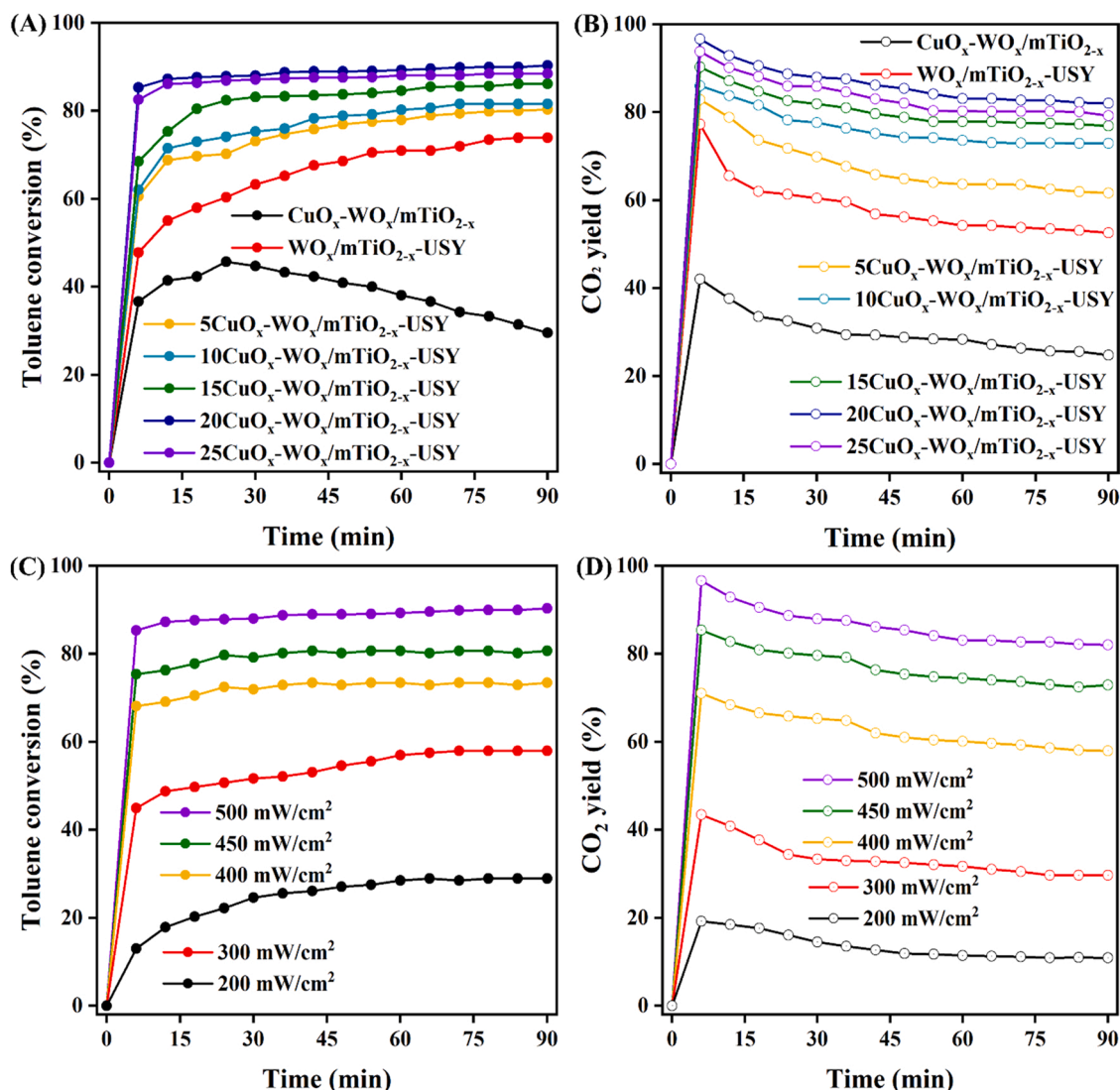
Fig. 4. Toluene conversion and (B) CO_2 yield of the samples for light-driven photothermal catalytic oxidation of toluene under 500 mW/cm^2 of light intensity; Toluene conversion (C) and CO_2 yield (D) over 20CuO$_x$-WO$_x$/mTiO$_{2-x}$-USY under the irradiation of simulated sunlight with different intensities (200 ppm, 5 vol% H$_2$O and WHSV = 26,000 mL g^{-1} h^{-1}).

yCuO$_x$-WO$_x$/mTiO$_{2-x}$-USY from 600 to 2400 nm can be attributed to the LSPR effect of the metallic Cu nanoparticles and low valence W^{5+} state suggesting the optical synergetic effect [40,41]. Therefore, the strong light absorption can be attributed to the presence of oxygen vacancies, Ti^{3+}, W^{5+}, and Cu$^+$/Cu^{2+} species.

The absorptance (a) % was calculated to determine how the addition of metal oxides improved capturing of photons across the light spectrum. Based on Table 1, the pure USY exhibited a light absorptance of 12.5%, whereas the unsupported CuO$_x$-WO$_x$/mTiO$_{2-x}$ displayed an absorptance of 92.8% indicating that the metal oxide is responsible for the material's inherent light absorption properties. A light absorption of 87.1% was observed for the optimized 20CuO$_x$-WO$_x$/mTiO$_{2-x}$-USY, suggesting strong photon absorption across the light spectrum. Hence the 20CuO$_x$-WO$_x$/mTiO$_{2-x}$-USY can efficiently absorb and convert photons into thermal energy that can trigger and drive the toluene oxidation reaction.

Previous studies have established the importance of efficient localized heat generation under irradiation for the achievement of high light-driven photothermal performance [42]. The thermal couple provides temperature evolution profiles on catalyst layers (Fig. 7B), and the

following sequence has been observed: 25CuO$_x$-WO$_x$/mTiO$_{2-x}$-USY > 20CuO$_x$-WO$_x$/mTiO$_{2-x}$-USY 20 > 15CuO$_x$-WO$_x$/mTiO$_{2-x}$-USY > 10 CuO$_x$-WO$_x$/mTiO$_{2-x}$-USY > 5CuO$_x$-WO$_x$/mTiO$_{2-x}$-USY > WO$_x$/mTiO$_{2-x}$-USY, which agrees with the UV-Vis-IR absorption spectra and adsorption coefficient analysis. Consequently, it can be inferred that the strong light absorption results in the incremental increase of catalyst surface temperature, thereby providing sufficient localized thermal energy to induce the catalytic oxidation of toluene.

To gain more insight into the influence of light on the activity and mobility of oxygen species present over the surface of 20CuO$_x$-WO$_x$/mTiO$_{2-x}$-USY, temperature-programmed desorption experiments of helium (He-TPD) and oxygen (O$_2$-TPD) were performed respectively. As shown in Fig. 7C, the O$_2$-TPD displayed a higher oxygen peak intensity compared to He-TPD indicating that oxygen species during the adsorption process can enter the lattice of catalysts. After full spectra light pretreatment, more oxygen species are desorbed at lower temperatures during O$_2$-TPD, indicating that the oxygen species of the sample display higher activity and migration, which should be related to the existence of oxygen vacancies [35]. Hence 20CuO$_x$-WO$_x$/mTiO$_{2-x}$-USY possessed outstanding O$_2$ activation ability attributed to the presence of abundant
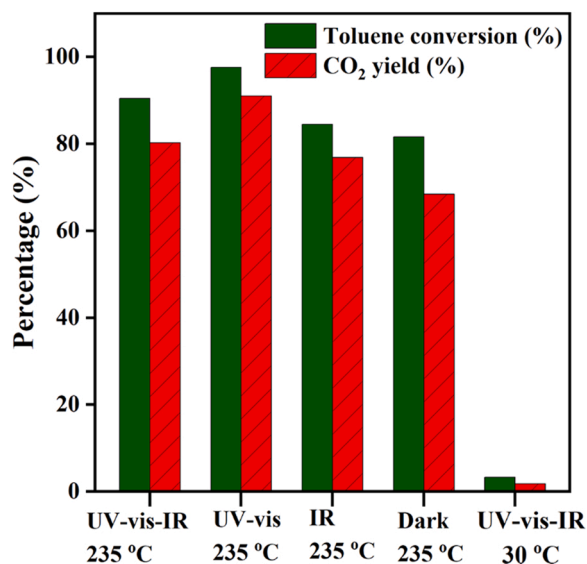
Fig. 5. Toluene conversion and CO_2 yield on $20CuO_x$-WO_x/$mTiO_{2-x}$-USY under the light irradiation of UV–vis–IR (abbreviated as UV–vis–IR, 235 °C), UV–vis at the same temperature (abbreviated as UV–vis, 235 °C), IR at the same temperature (abbreviated as IR, 235 °C), UV–vis–IR at 30 °C (abbreviated as UV–vis–IR, 30 °C) and in the dark at 235 °C (electric heating).

oxygen vacancies that promotes the oxidation of toluene.

In addition, to deeply investigate the role of different light in the whole light spectrum for toluene oxidation over $20CuO_x$-WO_x/$mTiO_{2-x}$-USY, the full light spectrum is subdivided into UV–vis and IR region, by placing cut-off filter and replacing the filter in the front of the lamp, as shown in Fig. S12. Compared to the O_2-TPD peak of $20CuO_x$-WO_x/$mTiO_{2-x}$-USY in the dark, the full light spectrum irradiation leads to a heightened oxygen desorption peak and a considerable shift to a lower temperature. The result reveals that the activity of the oxygen vacancies is enhanced, permitting the desorption of more active oxygen specie. The desorption peaks based on the light intensities follow the order: full spectrum (500 mW/cm^2) > UV–vis (λ < 800 nm, 365 mW/cm^2)> IR (λ > 800 nm, 180 mW/cm^2) > without light pretreatment. These results suggest the occurrence of higher O_2 activation activity on the $20CuO_x$-WO_x/$mTiO_{2-x}$-USY catalyst surface after light pretreatment.

Toluene MS-TPD were also conducted after pretreatment under full

light spectra and the mass spectrometry (MS) signals of toluene at $m/z = 91$ were recorded as shown in Fig. 7D. The influence of light on the activity of oxygen vacancies and lattice oxygen could be reflected by the intensity of the toluene desorption peaks. After light pretreatment, the toluene desorption peaks presented a higher intensity, indicating the desorption of more toluene over $20CuO_x$-WO_x/$mTiO_{2-x}$-USY [43]. Hence it can be concluded from these results that apart from acting as a source of heat, light energy equally plays a role in promoting the activation and migration of oxygen species on the catalyst surface, thereby accelerating the catalytic oxidation of toluene under light irradiation.

3.5. In situ DRIFTS analysis

Time-dependent *in-situ* DRIFTS measurements are carried out to illustrate the reaction mechanism and degradation pathway during the catalytic oxidation of toluene over $20CuO_x$-WO_x/$mTiO_{2-x}$-USY nanocomposites under heat and light irradiation as shown in Fig. 6 (A-D). The details of the bands related to the adsorbed and intermediate species were summarized in Table S4. As shown in Fig. 8A, during the toluene adsorption the peaks located at 3072 cm^{-1} and 3032 cm^{-1} could be attributed to the vibrational stretching of ν(C-H) in the aromatic ring of adsorbed toluene, while the peaks located at 2933 cm^{-1} and 2873 cm^{-1} were assigned to the symmetric and asymmetric extension of ν(C-H) bond in methylene (–CH_2), suggesting the breaking of the methyl (–CH_3) (3100–2800 cm^{-1}). The peak signals at 1604 and 1496 cm^{-1} were associated with the skeletal vibration of the ν(C=C) group in the toluene aromatic ring. (1610–1380 cm^{-1}) indicating the adsorption of toluene on $20CuW$-$mTiO_2$/USY [42].

The *in-situ* DRIFTS spectra under different reaction conditions were recorded to further highlight the role of light irradiation on the active oxygen species during the toluene degradation over $20CuO_x$-WO_x/$mTiO_{2-x}$-USY as shown in Fig. 8 (B-D). Fig. 7B shows the *in-situ* DRIFTS spectra of $20CuW$-$mTiO_2$/USY in the dark at 235 °C under toluene/N_2 flow. With reaction time, the intensity of the C–H in the benzene ring band (3072, 3034, and 2996 cm^{-1}), and benzoic acid (1604, 1497 cm^{-1}) was observed to increase with reaction time. This suggests the accumulation of aromantic intermediate species in the dark. However, these peaks reduced with light irradiation as shown in Fig. 7C, with strong peaks signals associated with intermediates such as benzoic acid (1600–1800 cm^{-1}) and benzaldehyde (1653 and 1646 cm^{-1}), as well as weak carboxylate (1540 and 1520 cm^{-1}) were observed after light irradiation has been introduced under the same reaction environment
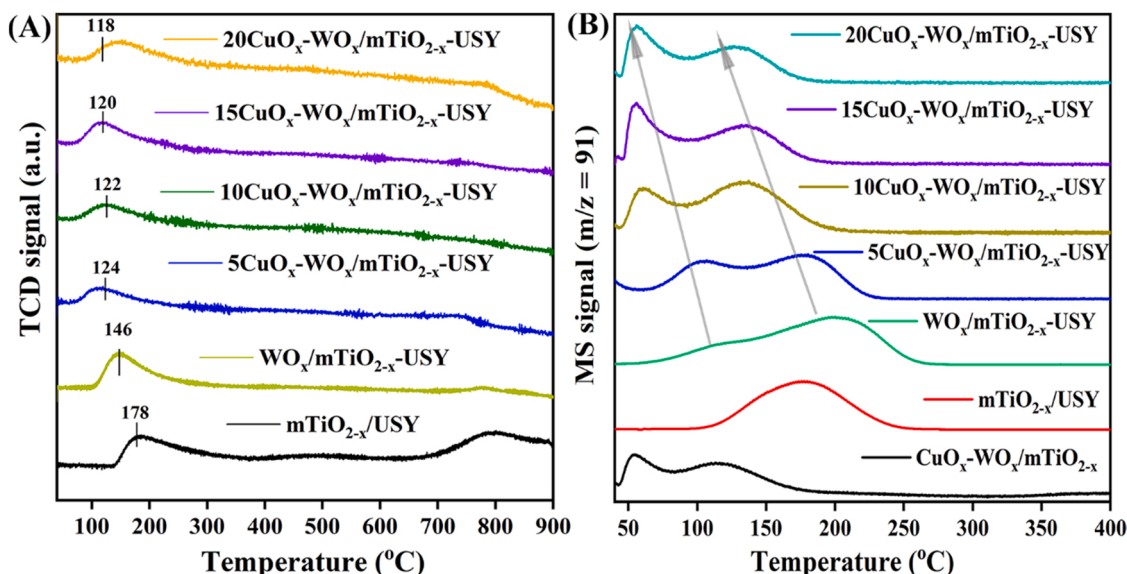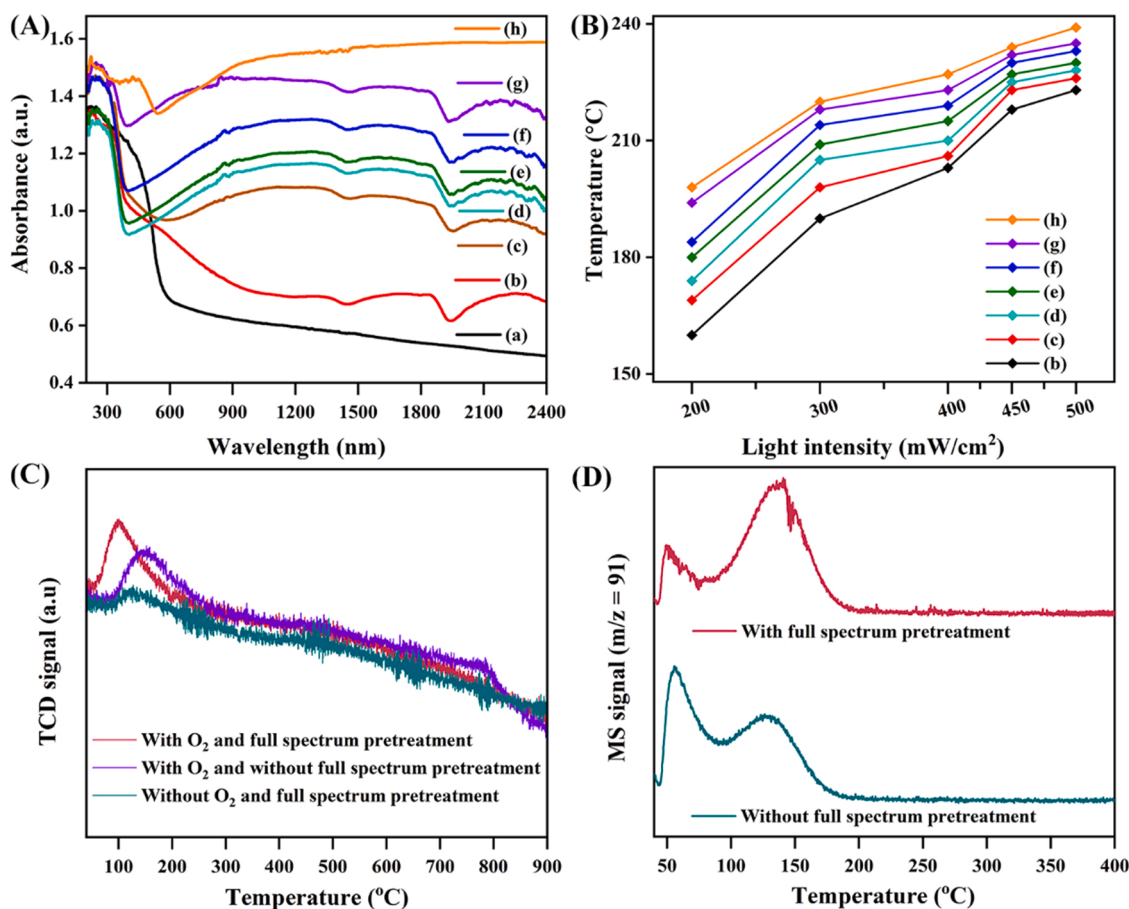

Fig. 6. (A) O_2-TPD curves and (B) Toluene-TPD-MS profiles ($m/z = 91$, toluene) of different samples.

Fig. 7. (A) UV–Vis-IR absorption spectra, (B) Equilibrium surface temperatures under different light intensities of (a) $mTiO_{2-x}$-USY, (b) $WO_x/mTiO_{2-x}$-USY, (c) $5CuO_x$-$WO_x/mTiO_{2-x}$-USY, (d) $10CuO_x$-$WO_x/mTiO_{2-x}$-USY, (e) $15CuO_x$-$WO_x/mTiO_{2-x}$-USY, (f) $20CuO_x$-$WO_x/mTiO_{2-x}$-USY, (g) $25CuO_x$-$WO_x/mTiO_{2-x}$-USY, and (h) CuO_x-$WO_x/mTiO_{2-x}$, (C) He-TPD and O_2-TPD profiles of $20CuO_x$-$WO_x/mTiO_{2-x}$-USY with and without full spectrum pretreatment, (D) Toluene-TPD-MS profiles ($m/z = 91$, toluene) of $20CuO_x$-$WO_x/mTiO_{2-x}$-USY with and without full spectrum pretreatment.

(235 °C and N_2 flow) [44]. In the meantime, the enhanced signal intensity of carbon dioxide at 2360 and 2321 cm^{-1} can be observed.

With the introduction of O_2 into the IR cell, the exhausted active surface oxygen was refilled leading to the rapid oxidation of adsorbed intermediates and the complete oxidation of toluene on the material surface. These results demonstrate that the complete catalytic oxidation of toluene required the synergistic participation of both lattice oxygen and adsorbed oxygen as depicted in Fig. 8D. Therefore, according to the *in-situ* DRIFT analysis, after toluene adsorption, the C-H bonds of the benzene ring and methyl group are oxidized to CO_2 and H_2O with benzaldehyde and benzoic acid as the major reaction intermediates. The proposed reaction mechanism is summarized in Fig. 9.

Interestingly, toluene oxidation over $WO_x/mTiO_{2-x}$-USY resulted in IR peaks with different intensities (Fig. S13). During adsorption at 30 °C, 3072, 3042, 2934 and 2882 cm^{-1} were observed due to accumulation and asymmetric stretching of C−H of the benzene ring and methylene group respectively as shown in Fig. S13 (A). With the elevation of surface temperatures to 223 °C (Fig. S13 (B), some weak peaks at around 1800–1600 cm^{-1} could be ascribed to the generation of benzoquinone and or other ketone species due to the opening of the benzene ring [44, 45]. The buildup of aromatic species on the catalyst surface was reduced slightly in the presence of light irradiation (Fig. S13 (C)), with the IR peaks around 1800–1600 cm^{-1} and 2348 cm^{-1} was associated with the production of benzoic species and CO_2. Consequently, the synergistic interaction between CuO_x-WO_x bimetal oxides increased the oxidation of toluene over $20CuO_x$-$WO_x/mTiO_{2-x}$-USY nanocomposites. Additionally, D-band centers of CuO_x favoured the adsorption of O_2 and cleavage of the O=O bond [46]. while the presence of active Cu^+/Cu^{2+} and

W^{5+}/W^{6+} redox pairs was critical for promoting continuous oxidation [47]. Thus, compared to $WO_x/mTiO_{2-x}$-USY, the superior performance of $20CuO_x$-$WO_x/mTiO_{2-x}$-USY for the light-driven photothermal catalytic degradation of toluene can be attributed to strong light absorption, abundant oxygen vacancies and an active $Cu^+\leftrightarrow Cu^{2+}$ and $W^{5+}\leftrightarrow W^{6+}$ redox couple.

From the above discussion, the light-driven photothermal catalytic oxidation of toluene over $20CuO_x$-$WO_x/mTiO_{2-x}$-USY complies with the Mars-van Krevelen mechanism where the lattice oxygen reacts with adsorbed VOC molecule, followed by the formation oxygen vacancy subsequent replenishing of reduced metal oxides and oxygen vacancy by gaseous molecular oxygen [16]. As demonstrated by XPS and O_2-TPD experiments, the $20CuO_x$-$WO_x/mTiO_{2-x}$-USY possess abundant oxygen vacancies and improved oxygen mobility by the incorporation of CuO_x-WO_x metal oxide into the $mTiO_2$/USY lattice and subsequent hydrogenation treatment. These properties contribute to the rapid oxidation of adsorbed toluene molecules to CO_2 and H_2O. Furthermore, the abundance of oxygen vacancies facilitates the activation of gaseous oxygen and the continuous generation of active oxygen species.

3.6. Stability test

For industrial applications, durability is one of the most important parameters for catalysts. On-stream toluene oxidation was investigated in the absence and presence of 5 vol% water vapour. In dry air, the $20CuO_x$-$WO_x/mTiO_{2-x}$-USY catalysts exhibit high stability with a slight decrease in a 12 h continuous test under humid air. The photothermal catalyst achieved toluene conversion and CO_2 yield of 89.3% and 77.
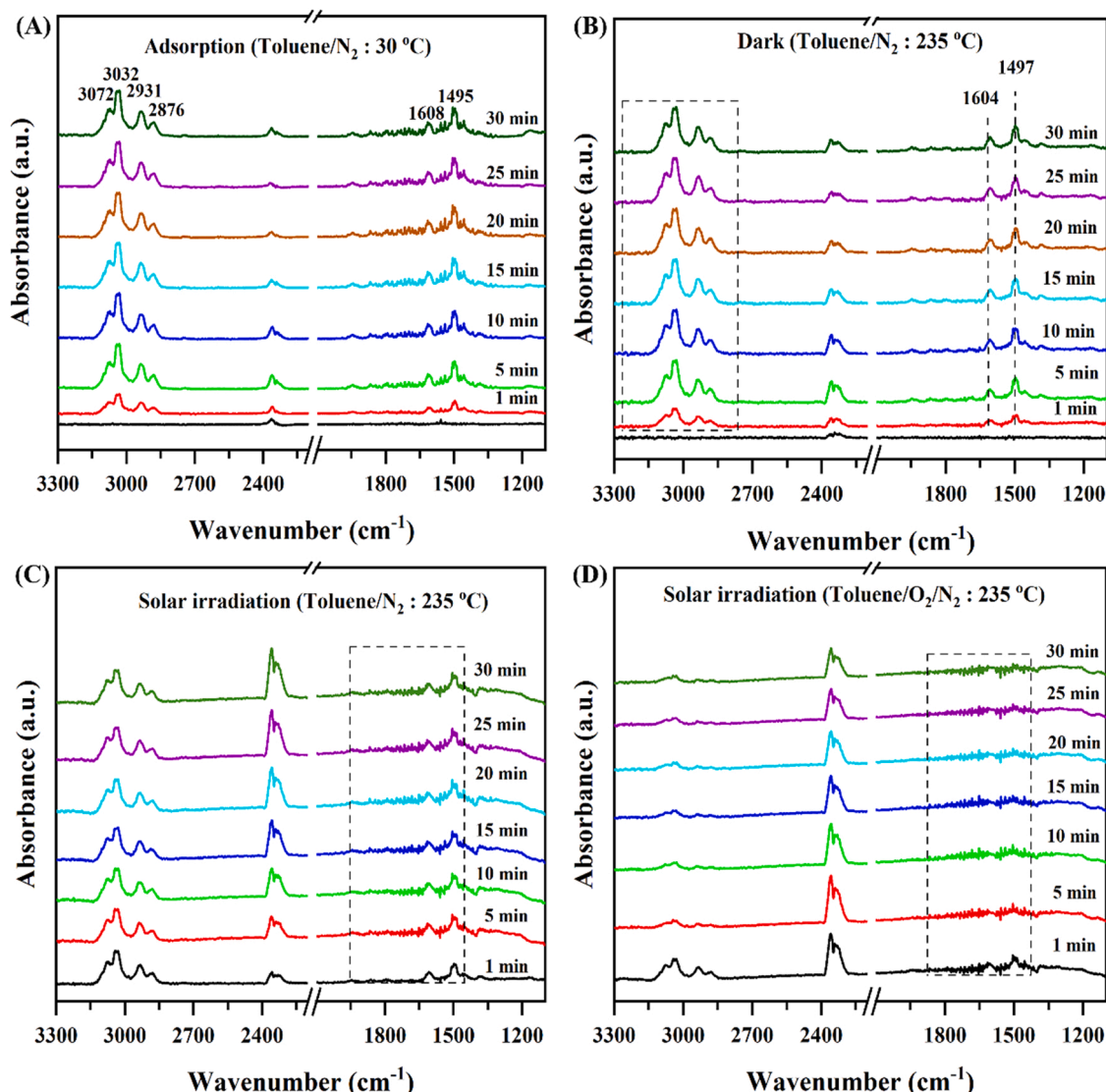
Fig. 8. Time-dependent *in-situ* DRIFTS spectra of toluene oxidation over $20CuO_x$-WO_x/$mTiO_{2-x}$-USY; (A) adsorption under toluene/He flow at 30 °C, (B) reaction in dark at 235 °C under N_2 flow, (C) reaction under light irradiation at 235 °C under N_2 flow, (D) reaction under light irradiation of at 235 °C in presence O_2/N_2.
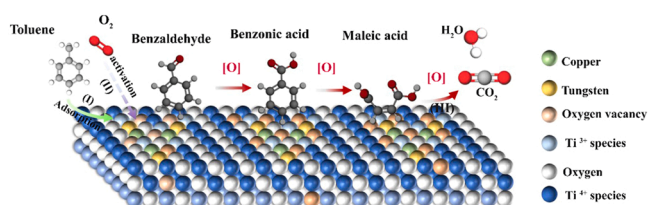

Fig. 9. Proposed reaction mechanism for toluene oxidation over the $20CuO_x$-WO_x/$mTiO_{2-x}$-USY catalysts.

0%, as shown in (Fig. S14 (A). The presence of water vapour in the feed stream is known to have negative effects on catalytic activities. Moreover, the stability of Cu under oxidizing conditions is a serious concern for long-term catalytic applications due to its sensitivity to oxidation. However, the $20CuO_x$-WO_x/$mTiO_{2-x}$-USY achieved a toluene conversion efficiency of 85.8% and CO_2 yield of 74.5% as depicted in Fig. 10A under humid air for 12 h. The cycle stability test was also carried out under humid and dry conditions for 10 cycles, as depicted in Fig. 10 (B) and Fig. S14 (B) with each cycle lasting for 90 mins. There was no significant decrease in the toluene conversion and CO_2 yield as depicted in

Fig. S14 (B) after 10 cycles, although the toluene conversion decreased slightly in the presence of water vapour as depicted in Fig. 10 (B). The above results suggests that $20CuO_x$-WO_x/$mTiO_{2-x}$-USY exhibits good catalytic stability.

To further explore the applicability of $20CuO_x$-WO_x/$mTiO_{2-x}$-USY, the activity of the catalyst for other typical VOCs such as benzene, o-xylene, ethyl benzene and ethyl acetate with an initial concentration of ~ 200 ppm has also been investigated under humid and dry conditions. Under humid conditions as shown as Fig. 10 (C and D), the conversion and CO_2 yield of the aromatic VOCs benzene, o-xylene and ethyl acetate exceeded 86.0% and 78.6% respectively. The $20CuO_x$-WO_x/$mTiO_{2-x}$-USY achieved a lower conversion and CO_2 yield of ethyl acetate of 80.0% and 71.3% which can be attributed to the stronger competitive adsorption of water molecules and ethyl acetate for limited adsorption sites. In the absence of water vapour, the photothermal conversion and CO_2 yield of the aromatic VOCs exceeded 90.0% and 80.9% respectively (Fig. S14 (C and D). The $20CuO_x$-WO_x/$mTiO_{2-x}$-USY achieved a conversion and CO_2 yield of 85.0% and 78.0% respectively. This above experiment results combined with the BET, EDX and XPS analysis, suggests that the presence of large specific surface area, active CuO_x-WO_x surface sites and abundant oxygen vacancies, promoted the adsorption and photothermal catalytic oxidation other VOCs, indicating
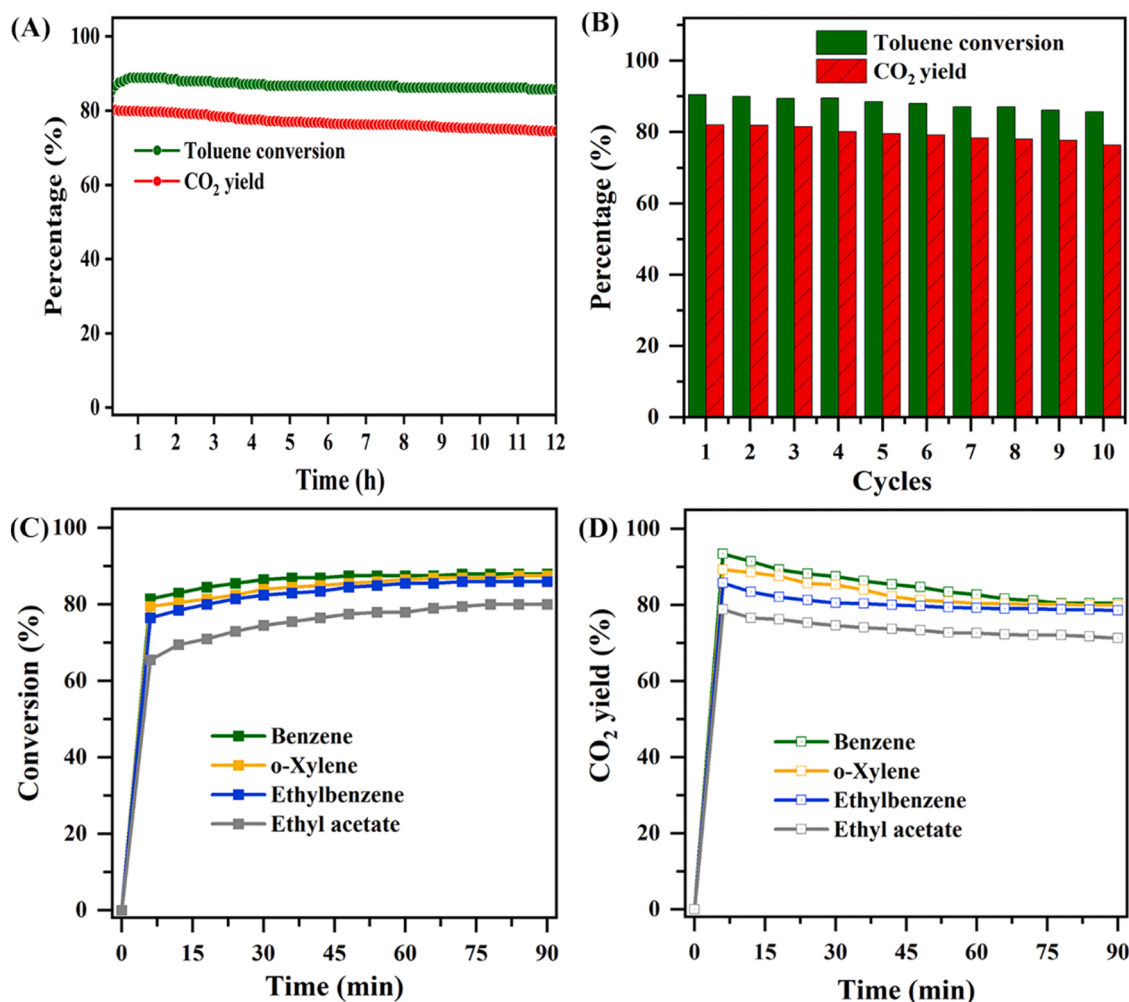
Fig. 10. Durability of 20CuO$_x$-WO$_x$/mTiO$_{2-x}$-USY for the light-driven photothermal catalytic oxidation of 200 ppm toluene during (A) 12 h long term continuous experiment under irradiation (500 mW/cm^2, 5 vol% H$_2$O, 15 mL/min) (B) 10 cycle tests under light irradiation with an intensity 500 mW/cm^2 in the presence of 5 vol% H$_2$O, with each reaction cycle lasting 90 mins (C) conversion, (D) CO$_2$ yield of benzene, o-xylene, ethyl benzene and ethyl acetate (200 ppm) over 20CuO$_x$-WO$_x$/mTiO$_{2-x}$-USY under light irradiation with an intensity 500 mW/ cm^2 in the presence of 5 vol% H$_2$O.

the wide applicability of 20CuO$_x$-WO$_x$/mTiO$_{2-x}$-USY.

By analyzing the Cu 2 P XPS spectra, the relative amount of Cu$^+$ was estimated by calculating the peak area ratio of Cu$^+$ to the total area of Cu species present, as displayed in Fig. 11(A). The Cu$^+$/(Cu$^+$+Cu^{2+}) ratio decreases from 0.49 for 20CuO$_x$-WO$_x$/mTiO$_{2-x}$-USY fresh samples to 0.43 and 0.42 after a long-term stability test under humid and dry conditions. Similarly, from the W 4 f XPS (Fig. 11B), the W^{5+}/ (W^{6+} + W^{5+}) ratio content decreased from 0.38 for fresh samples to 0.35 and 0.32 after the stability test under humid and dry conditions respectively. The enhanced surface amount of metal species under humid conditions can be attributed to the photoreduction of surface hydroxide species (OH$^-$) to form hydroxyl radical (•OH) and/or the reduction of oxidized elements by electrons trapped by the oxygen-vacant sites, thereby contributing to the reversible Cu$^+$ ↔ Cu^{2+} and W^{5+} ↔ W^{6+} cycle [48, 49]. Interestingly, from the O 1 s XPS spectra (Fig. 11C), the concentration of oxygen vacancies was relatively the same for fresh and used samples, with no apparent difference in the binding energies suggesting the good chemical stability of 20CuO$_x$-WO$_x$/mTiO$_{2-x}$-USY. Besides no obvious XRD pattern change was observed for the catalyst before and after the 12 h long-term stability test under humid conditions, as displayed in (Fig. 11(D), thereby providing strong evidence of the structural stability of the catalyst. Furthermore, the result from the stability suggests that 20CuO$_x$-WO$_x$/mTiO$_{2-x}$-USY possesses good durability and an efficient redox cycle for the enhanced light-driven photothermal
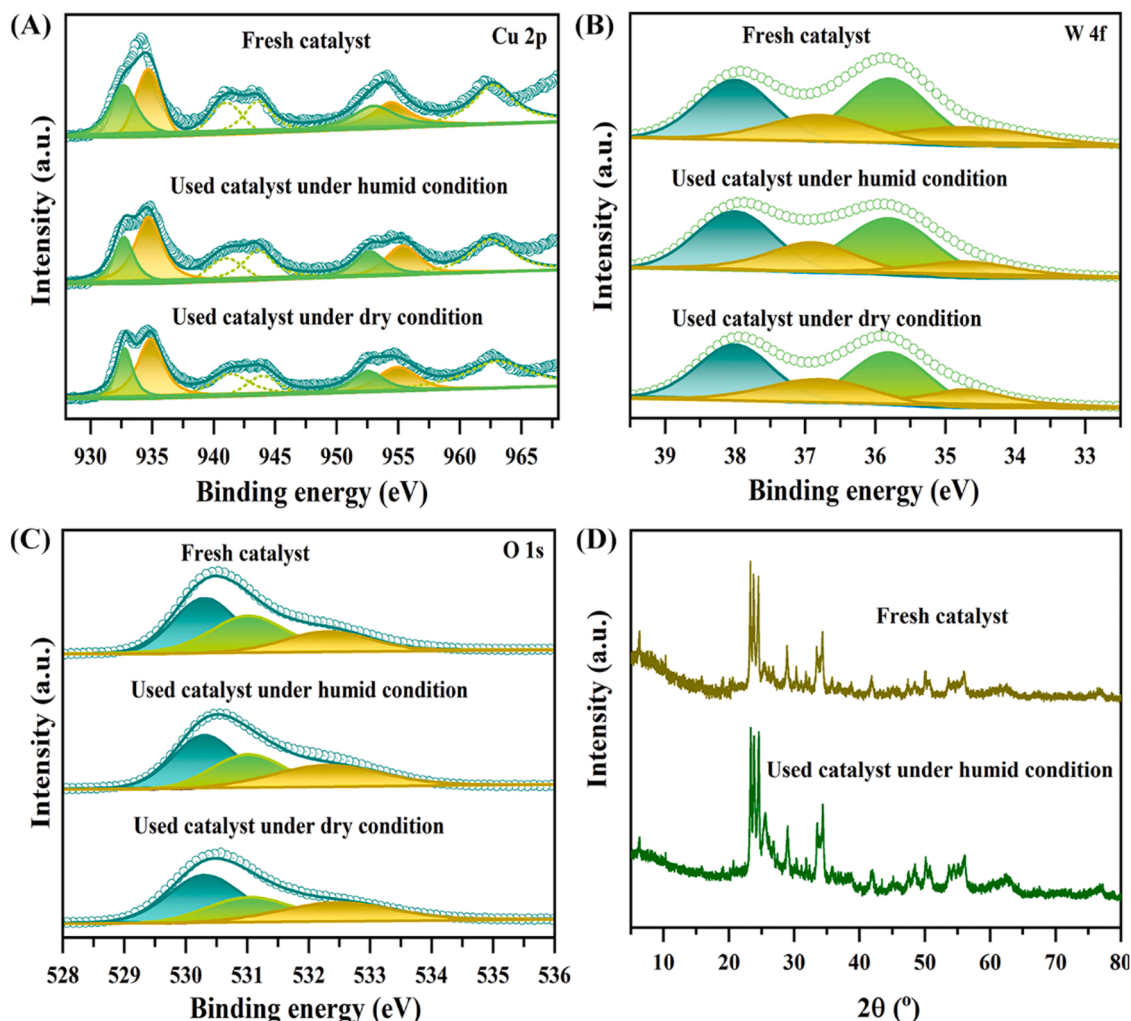
catalytic oxidation of toluene.

4. Conclusions

The loading of CuO$_x$ and WO$_x$ metal oxides on a titanium-modified USY support provides an efficient route for active components to accumulate light-induced electrons and heat generation under full light irradiation. The optimized 20CuO$_x$-WO$_x$/mTiO$_{2-x}$-USY exhibited the best catalytic activity for the degradation of toluene due to the strong light absorption, large surface area, abundant oxygen vacancies, as well as the presence of active Cu$^+$/Cu^{2+} and W^{5+}/W^{6+} redox pairs. Furthermore, investigation of temperature-programmed desorption and *in situ* DRIFTS on 20CuO$_x$-WO$_x$/mTiO$_{2-x}$-USY reveals that the CuO$_x$-WO$_x$ synergy promotes the activation of molecular oxygen and mobility of oxygen species which accelerates the oxidation of toluene and reaction intermediates. In general, the present study offers a new perspective for an energy-efficient light-driven photothermal catalytic removal of VOCs over the supported plasmonic metal oxide catalysts.

CRediT authorship contribution statement

Ehiaghe Agbovhimen Elimian: Conceptualization, Data curation, Formal analysis, Investigation, Methodology, Writing – original draft. **Meng Zhang** Methodology, Resources, Writing – review & editing.

Fig. 11. (A) Cu 2p, (B) W 4 f, (C) O 1 s XPS spectra of fresh and used 20CuO$_x$-WO$_x$/mTiO$_{2-x}$-USY samples after 12 h toluene light-driven thermal catalytic oxidation, (D) XRD pattern of fresh and used 20CuO$_x$-WO$_x$/mTiO$_{2-x}$-USY after stability test under humid condition.

Qiang Li: Methodology, Resources, Writing – review & editing. **Jing Chen:** Methodology, Writing – review & editing. **Yong Sun:** Supervision, Project administration. **Jun He:** Supervision, Project administration. **Hongpeng Jia:** Conceptualization, Supervision, Writing – review & editing, Project administration, Funding acquisition.

Declaration of Competing Interest

The authors declare that they have no known competing financial interests or personal relationships that could have appeared to influence the work reported in this paper.

Data Availability

Data will be made available on request.

Acknowledgments

Appendix A. Supporting information

Supplementary data associated with this article can be found in the online version at doi:10.1016/j.apcatb.2023.122702.

References

[1] S. Gu, A. Guenther, C. Faiola, Effects of anthropogenic and biogenic volatile organic compounds on Los Angeles air quality, Environ. Sci. Technol. 55 (2021) 12191–12201, https://doi.org/10.1021/acs.est.1c01481.

[2] Y. Guo, M. Wen, G. Li, T. An, Recent advances in VOC elimination by catalytic oxidation technology onto various nanoparticles catalysts: a critical review, Appl. Catal. B: Environ. 281 (2021), 119447, https://doi.org/10.1016/j.apcatb.2020.119447.

[3] M. Stucchi, C.L. Bianchi, C. Pirola, S. Vitali, G. Cerrato, S. Morandi, C. Argirusis, G. Sourkouni, P.M. Sakkas, V. Capucci, Surface decoration of commercial micro-sized TiO₂ by means of high energy ultrasound: A way to enhance its photocatalytic activity under visible light, Appl. Catal. B: Environ. 178 (2015) 124–132, https://doi.org/10.1016/j.apcatb.2014.10.004.

[4] S. Linic, P. Christopher, D.B. Ingram, Plasmonic-metal nanostructures for efficient conversion of solar to chemical energy, Nat. Mater. 10 (2011) 911–921, https://doi.org/10.1038/nmat3151.

[5] J. He, D. Chen, N. Li, Q. Xu, H. Li, J. He, J. Lu, Controlled fabrication of mesoporous ZSM-5 zeolite-supported PdCu alloy nanoparticles for complete oxidation of toluene, Appl. Catal. B: Environ. 265 (2020) 118560, https://doi.org/10.1016/j.apcatb.2019.118560.

[6] M. Sayed, L. Zhang, J. Yu, Plasmon-induced interfacial charge-transfer transition prompts enhanced CO₂ photoreduction over Cu/Cu₂O octahedrons, Chem. Eng. J. 397 (2020), 125390, https://doi.org/10.1016/j.jcat.2012.07.026.

[7] U. Menon, H. Poelman, V. Bliznuk, V.V. Galvita, D. Poelman, G.B. Marin, Nature of the active sites for the total oxidation of toluene by CuOCeO₂/Al₂O₃, J. Catal. 295 (2012) 91–103, https://doi.org/10.1016/j.jcat.2012.07.026.

[8] Y. Qi, Z. Yang, Y. Jiang, H. Han, T. Wu, L. Wu, J. Liu, Z. Wang, F. Wang, Platinum−copper bimetallic nanoparticles supported on TiO₂ as catalysts for photo−thermal catalytic toluene combustion, ACS Appl. Nano Mater. 5 (2022) 1845–1854, https://doi.org/10.1021/acsanm.1c03429.

[9] H. Tang, Z. Tang, J. Bright, B. Liu, X. Wang, G. Meng, N. Wu, Visible-light localized surface plasmon resonance of WO₃₋ₓ nanosheets and its photocatalysis driven by plasmonic hot carriers, ACS Sustain. Chem. Eng. 9 (2021) 1500–1506, https://doi.org/10.1021/acssuschemeng.0c08140.

[10] Y. Li, C. Wang, H. Zheng, F. Wan, F. Yu, X. Zhang, Y. Liu, Surface oxygen vacancies on WO₃ contributed to enhanced photothermo-synergistic effect, Appl. Surf. Sci. 391 (2017) 654–661, https://doi.org/10.1016/j.apsusc.2016.07.042.

[11] R. Taghavi, S. Rostamnia, M. Farajzadeh, H. Karimi-Maleh, J. Wang, D. Kim, H. W. Jang, R. Luque, R.S. Varma, M. Shokouhimehr, Magnetite metal–organic frameworks: applications in environmental remediation of heavy metals, organic contaminants, and other pollutants, Inorg. Chem. 61 (2022) 15747–15783, https://doi.org/10.1021/acs.inorgchem.2c01939.

[12] R. Nasiri, B. Gholipour, M. Nourmohammadi, Z. Karimi, S. Doaee, R. Taghavi, S. Rostamnia, E. Zarenezhad, F. Karimi, T. Kavetskyy, O. Smutok, A. Kiv, V. Soloviev, S. Khaksar, A.S. Hamidi, Mesoporous hybrid organosilica for stabilizing Pd nanoparticles and aerobic alcohol oxidation through Pd hydride (Pd–H₂) species, Int. J. Hydrog. Energy (2022), https://doi.org/10.1016/j.ijhydene.2022.04.242.

[13] P. Hayati, Z. Mehrabadi, M. Karimi, J. Janczak, K. Mohammadi, G. Mahmoudi, F. Dadi, M.J.S. Fard, A. Hasanzadeh, S. Rostamnia, Photocatalytic activity of new nanostructures of an Ag(i) metal–organic framework (Ag-MOF) for the efficient degradation of MCPA and 2,4-D herbicides under sunlight irradiation, N. J. Chem. 45 (2021) 3408–3417, https://doi.org/10.1039/D0NJ02460K.

[14] B. Gholipour, A. Zonouzi, M. Shokouhimehr, S. Rostamnia, Integration of plasmonic AgPd alloy nanoparticles with single-layer graphitic carbon nitride as Mott-Schottky junction toward photo-promoted H₂ evolution, Sci. Rep. 12 (2022) 13583, https://doi.org/10.1038/s41598-022-17238-4.

[15] M.A. O'Neill, F.L. Cozens, N.P. Schepp, Photogeneration and migration of electrons and holes in zeolite NaY, J. Phys. Chem. B 105 (2001) 12746–12758, https://doi.org/10.1021/jp015518j.

[16] E.A. Elimian, M. Zhang, J. Chen, H. Jia, Y. Sun, J. He, Construction of Pt-mTiO₂/USY multifunctional catalyst enriched with oxygen vacancies for the enhanced light-driven photothermocatalytic degradation of toluene, Appl. Catal. B: Environ. 307 (2022) 121203, https://doi.org/10.1016/j.apcatb.2022.121203.

[17] R. Yu, Z. Zhao, S. Huang, W. Zhang, Cu-SSZ-13 zeolite–metal oxide hybrid catalysts with enhanced SO₂-tolerance in the NH₃-SCR of NOx, Appl. Catal. B: Environ. 269 (2020), 118825, https://doi.org/10.1016/j.apcatb.2020.118825.

[18] M. Zhu, B. Li, J.-M. Jehng, L. Sharma, J. Taborda, L. Zhang, E. Stach, I.E. Wachs, Z. Wu, J. Baltrusaitis, Molecular structure and sour gas surface chemistry of supported K₂O/WO₃/Al₂O₃ catalysts, Appl. Catal. B: Environ. 232 (2018) 146–154, https://doi.org/10.1016/j.apcatb.2018.03.044.

[19] M. Mafokoane, J. Seguel, R. García, J.N. Díaz de León, C. Sepúlveda, N. Escalona, Conversion of levulinic acid using CuO/WO₃₍ₓ₎-Al₂O₃ catalysts, Catal. Today 367 (2021) 310–319, https://doi.org/10.1016/j.cattod.2020.02.028.

[20] K. Thummavichai, L. Trimby, N. Wang, C.D. Wright, Y. Xia, Y. Zhu, Low temperature annealing improves the electrochromic and degradation behavior of tungsten oxide (WOₓ) thin films, J. Phys. Chem. C 121 (2017) 20498–20506, https://doi.org/10.1021/acs.jpcc.7b06300.

[21] T. Yu, X. Zhao, Z.X. Shen, Y.H. Wu, W.H. Su, Investigation of individual CuO nanorods by polarized micro-Raman scattering, J. Cryst. Growth 268 (2004) 590–595, https://doi.org/10.1016/j.jcrysgro.2004.04.097.

[22] F. Han, M. Yuan, S. Mine, H. Sun, H. Chen, T. Toyao, M. Matsuoka, K. Zhu, J. Zhang, W. Wang, T. Xue, Formation of highly active superoxide sites on CuO nanoclusters encapsulated in SAPO-34 for catalytic selective ammonia oxidation, ACS Catal. 9 (2019) 10398–10408, https://doi.org/10.1021/acscatal.9b02975.

[23] H. Einaga, Y. Teraoka, A. Ogata, Catalytic oxidation of benzene by ozone over manganese oxides supported on USY zeolite, J. Catal. 305 (2013) 227–237, https://doi.org/10.1016/j.jcat.2013.05.016.

[24] H. Song, Y. Li, Z. Lou, M. Xiao, L. Hu, Z. Ye, L. Zhu, Synthesis of Fe-doped WO₃ nanostructures with high visible-light-driven photocatalytic activities, Appl. Catal. B: Environ. 166–167 (2015) 112–120, https://doi.org/10.1016/j.apcatb.2014.11.020.

[25] S.M. Waziri, A.M. Aitani, S. Al-Khattaf, Transformation of toluene and 1,2,4-Tri-methylbenzene over ZSM-5 and mordenite catalysts: a comprehensive kinetic model with reversibility, Ind. Eng. Chem. Res. 49 (2010) 6376–6387, https://doi.org/10.1021/ie100527x.

[26] Y. Hu, M. Nie, P. Hong, J. He, Y. Li, K. Zhang, D. Yang, L. Jiang, J. Liu, L. Kong, Defect-engineered WO₃₋ₓ@MoS₂ hollow tube exhibiting enhanced Fenton-like and photocatalytic activities via electric field rearrangement and band alignment, Appl. Catal. B: Environ. 320 (2023), 122013, https://doi.org/10.1016/j.apcatb.2022.122013.

[27] T. Zhao, Z. Xing, Z. Xiu, Z. Li, P. Chen, Q. Zhu, W. Zhou, Synergistic effect of surface plasmon resonance, Ti³⁺ and oxygen vacancy defects on Ag/MoS₂/TiO₂₋ₓ ternary heterojunctions with enhancing photothermal catalysis for low-temperature wastewater degradation, J. Hazard. Mater. 364 (2019) 117–124, https://doi.org/10.1016/j.jhazmat.2018.09.097.

[28] M. Hu, Z. Xing, Y. Cao, Z. Li, X. Yan, Z. Xiu, T. Zhao, S. Yang, W. Zhou, Ti³⁺ self-doped mesoporous black TiO₂/SiO₂/g-C₃N₄ sheets heterojunctions as remarkable

[29] visible-lightdriven photocatalysts, Appl. Catal. B: Environ. 226 (2018) 499–508, https://doi.org/10.1016/j.apcatb.2017.12.069.

[29] Y. Li, Z. Tang, J. Zhang, Z. Zhang, Defect engineering of air-treated WO₃ and its enhanced visible-light-driven photocatalytic and electrochemical performance, J. Phys. Chem. C 120 (2016) 9750–9763, https://doi.org/10.1021/acs.jpcc.6b00457.

[30] B. Pereda-Ayo, U. De La Torre, M.J. Illán-Gómez, A. Bueno-López, J.R. González-Velasco, Role of the different copper species on the activity of Cu/zeolite catalysts for SCR of NOx with NH₃, Appl. Catal. B Environ. 147 (2014) 420–428, https://doi.org/10.1016/j.apcatb.2013.09.010.

[31] W. Shi, X. Guo, C. Cui, K. Jiang, Z. Li, L. Qu, J.-C. Wang, Controllable synthesis of Cu₂O decorated WO₃ nanosheets with dominant (0 0 1) facets for photocatalytic CO₂ reduction under visible-light irradiation, Appl. Catal. B: Environ. 243 (2019) 236–242, https://doi.org/10.1016/j.apcatb.2018.09.076.

[32] J. Hou, J. Hu, L. Chang, J. Wang, Z. Zeng, D. Wu, X. Cui, W. Bao, J. Yao, Synergistic effects between highly dispersed CuOₓ and the surface Cu-[Oₓ]-Ce structure on the catalysis of benzene combustion, J. Catal. 408 (2022) 9–23, https://doi.org/10.1016/j.jcat.2022.02.012.

[33] Y. Zhang, J. Zhao, H. Wang, B. Xiao, W. Zhang, X. Zhao, T. Lv, M. Thangamuthu, J. Zhang, Y. Guo, J. Ma, L. Lin, J. Tang, R. Huang, Q. Liu, Single-atom Cu anchored catalysts for photocatalytic renewable H₂ production with a quantum efficiency of 56, Nat. Commun. 13 (2022) 58, https://doi.org/10.1038/s41467-021-27698-3.

[34] C. Feng, L. Tang, Y. Deng, J. Wang, W. Tang, Y. Liu, Z. Chen, J. Yu, J. Wang, Q. Liang, Synthesis of branched WO₃@W₁₈O₄₉ homojunction with enhanced interfacial charge separation and full-spectrum photocatalytic performance, Chem. Eng. J. 389 (2020) 124474, https://doi.org/10.1016/j.cej.2020.124474.

[35] Y. Xu, Z. Qu, Y. Ren, C. Dong, Enhancement of toluene oxidation performance over Cu–Mn composite oxides by regulating oxygen vacancy, Appl. Surf. Sci. 560 (2021), 149983, https://doi.org/10.1016/j.apsusc.2021.149983.

[36] Y. Zhang, Y. Li, Z. Zeng, J. Hu, Y. Hou, Z. Huang, Synergically engineering Cu⁺ and oxygen vacancies in CuMn₂O₄ catalysts for enhanced toluene oxidation performance, Mol. Catal. 517 (2022), 112043, https://doi.org/10.1016/j.mcat.2021.112043.

[37] K. Yu, J. Deng, Y. Shen, A. Wang, L. Shi, D. Zhang, Efficient catalytic combustion of toluene at low temperature by tailoring surficial Pt⁰ and interfacial Pt-Al(OH)ₓ species, IScience 24 (2021), 102689, https://doi.org/10.1016/j.isci.2021.102689.

[38] Z. Guo, W. Hao, J. Ma, R. Li, Probing the pore structure of hierarchical EU-1 zeolites by adsorption of large molecules and through catalytic reaction, J. Chem. Res 45 (2020) 187–193, https://doi.org/10.1177/1747519820936594.

[39] J. Yan, T. Wang, G. Wu, W. Dai, N. Guan, L. Li, J. Gong, Tungsten oxide single crystal nanosheets for enhanced multichannel solar light harvesting, Adv. Mater. 27 (2015) 1580–1586, https://doi.org/10.1002/adma.201404792.

[40] L. Zhang, C. Jia, S. He, Y. Zhu, Y. Wang, Z. Zhao, X. Gao, X. Zhang, Y. Sang, D. Zhang, X. Xu, H. Liu, Hot hole enhanced synergistic catalytic oxidation on Pt-Cu alloy clusters, Adv. Sci. 4 (2017) 1600448, https://doi.org/10.1002/advs.201600448.

[41] A.K.L. Sajjad, S. Shamaila, B. Tian, F. Chen, J. Zhang, One step activation of WOₓ/TiO₂ nanocomposites with enhanced photocatalytic activity, Appl. Catal. B: Environ. 91 (2009) 397–405, https://doi.org/10.1016/j.apcatb.2009.06.005.

[42] J. Wang, X. Gao, Y. Wang, S. Wang, Z. Xie, B. Yang, Z. Zhang, Z. Yang, L. Kang, W. Yao, Multifunctional core-double-shell C@MnO@TiO₂ catalysts with enhanced full-light conversion for the highly efficient photothermal oxidation of toluene, Appl. Catal. B: Environ. 317 (2022), 121789, https://doi.org/10.1016/j.apcatb.2022.121789.

[43] Y. Feng, L. Wei, Z. Wang, Y. Liu, H. Dai, C. Wang, H.-C. Hsi, E. Duan, Y. Peng, J. Deng, Boosting catalytic stability for VOCs removal by constructing PtCu alloy structure with superior oxygen activation behavior, J. Hazard. Mater. 439 (2022), 129612, https://doi.org/10.1016/j.jhazmat.2022.129612.

[44] J. Zhong, Y. Zeng, D. Chen, S. Mo, M. Zhang, M. Fu, J. Wu, Z. Su, P. Chen, D. Ye, Toluene oxidation over Co³⁺-rich spinel Co₃O₄: Evaluation of chemical and by-product species identified by in situ DRIFTS combined with PTR-TOF-MS, J. Hazard. Mater. 386 (2020) 121957, https://doi.org/10.1016/j.jhazmat.2019.121957.

[45] C. Liang, C. Li, Y. Zhu, X. Du, Y. Zeng, Y. Zhou, J. Zhao, S. Li, X. Liu, Q. Yu, Y. Zhai, Light-driven photothermal catalysis for degradation of toluene on CuO/TiO₂ composite: dominating photocatalysis and auxiliary thermalcatalysis, Appl. Surf. Sci. 601 (2022), 154144, https://doi.org/10.1016/j.apsusc.2022.154144.

[46] L. Kang, B. Wang, Q. Bing, M. Zalibera, R. Büchel, R. Xu, Q. Wang, Y. Liu, D. Gianolio, C.C. Tang, E.K. Gibson, M. Danaie, C. Allen, K. Wu, S. Marlow, L. dong Sun, Q. He, S. Guan, A. Savitsky, J.J. Velasco-Vélez, J. Callison, C.W.M. Kay, S.E. Pratsinis, W. Lubitz, J. yao Liu, F.R. Wang, Adsorption and activation of molecular oxygen over atomic copper(I/II) site on ceria, Nat. Commun. 11 (2020) 17–19, https://doi.org/10.1038/s41467-020-17852-8.

[47] Y. Zeng, K.-G. Haw, Z. Wang, Y. Wang, S. Zhang, P. Hongmanorom, Q. Zhong, S. Kawi, Double redox process to synthesize CuO–CeO₂ catalysts with strong Cu–Ce interaction for efficient toluene oxidation, J. Hazard. Mater. 404 (2021), 124088, https://doi.org/10.1016/j.jhazmat.2020.124088.

[48] J. Kong, C. Jiang, Z. Rui, S. Liu, F. Xian, W. Ji, H. Ji, Photothermocatalytic synergistic oxidation: an effective way to overcome the negative water effect on supported noble metal catalysts for VOCs oxidation, Chem. Eng. J. 397 (2020), 125485, https://doi.org/10.1016/j.cej.2020.125485.

[49] Y. Hao, Y. Ma, X. Zhang, J. Li, S. Wang, X. Chen, F. Li, Unraveling the importance between electronic intensity and oxygen vacancy on photothermocatalytic toluene oxidation over CeO₂, Chem. Eng. J. 433 (2022), 134619, https://doi.org/10.1016/j.cej.2022.134619.